

Performance Analysis and Power Allocation for Covert Mobile Edge Computing With RIS-Aided NOMA

Yanyu Cheng, Jianyuan Lu, Dusit Niyato, *Fellow, IEEE*, Biao Lyu, Minrui Xu, and Shunmin Zhu

Abstract—Mobile edge computing (MEC) is a key enabling technology for the sixth-generation (6G) wireless networks. In this paper, we apply covert communications to MEC to prevent information leakage, where two candidate technologies of 6G, reconfigurable intelligent surface (RIS) and non-orthogonal multiple access (NOMA), are adopted. Specifically, a legitimate transmitter sends messages to a pair of legitimate receivers, while a warden aims to detect whether the legitimate transmission exists. We can hide the existence of the stronger-signal receiver's transmission from a warden by exploiting the nature of NOMA, and we use a jammer to further hide this existence. We first analyze the performance for the case of fixed power allocation between the legitimate transmitters and the jammer. The closed-form expressions for the minimum detection error probability and ergodic public/covert rates are derived. Then, we design a reinforcement learning (RL)-based power-allocation optimization algorithm that maximizes the sum rate while ensuring covertness, by optimizing the power allocation between the transmitters and the jammer. Simulation results validate the correctness of our analysis and demonstrate the covertness of the proposed scheme. Furthermore, the performance with the RL-based algorithm is significantly better than the baseline scheme, which reflects the effectiveness of our proposed algorithm.

Index Terms—Covert communications, mobile edge computing, non-orthogonal multiple access, reconfigurable intelligent surface, reinforcement learning.

1 INTRODUCTION

MOBILE devices, such as smart phones and tablets, have been indispensable communication tools for business, social networking, and personal entertainment [2]. However, more and more computation-intensive mobile applications are developed for the convenience and experience of users, such as interactive online gaming, object recognition, and voice control [3].

These applications are severely constrained by the limited computing, storage, and energy resources on mobile devices. Mobile edge computing (MEC) technology is proposed to solve the above problem, which is a new paradigm as an enhancement of mobile cloud computing [4]. The key idea of an MEC network is to distribute computing resources closer to the mobile users by deploying servers at the “edge” of the network, namely mobile edge nodes (MENs) [5]. Therefore, MEC networks allow mobile users to access content and resources from nearby MENs instead of downloading content from cloud servers (CS), which can reduce service latency and alleviate network congestion on backhaul links [6]. As a result, MEC is a candidate technology for future communication networks.

Since a large amount of confidential and sensitive data are transmitted during the task offloading and computational result feedback in MEC, network security has become more important [7]. Physical layer security has been adopted to protect MEC from information leakage, which exploits the intrinsic randomness of noise and fading channels [8]. However, the existing widely-used approach is information-theoretic secrecy, which is not enough to protect communication content in some circumstances. The communication itself usually needs to be hidden from detection [8]. Therefore, covert communications are proposed to covertly transmit information from a legitimate transmitter to its legitimate receiver, with a negligible probability of being detected by a warden [9]. As a result, covert task offloading and computational result feedback can be realized in MEC.

It is well known that MEC will be a key enabling technology for the sixth-generation (6G) networks. From the physical-layer perspective, reconfigurable intelligent surfaces (RISs) and non-orthogonal multiple access (NOMA) have been recognized as two very promising technologies for 6G [10]. 6G use cases demand capacity, and this requires a large spectrum bandwidth, i.e., using a higher frequency spectrum such as terahertz communications [11]. However, if the frequency is higher, the coverage will be lower. As a result, small coverage becomes a problem for future MEC systems. Fortunately, RISs are a cost-effective solution to improve cell coverage by assisting the transmission of cell-edge users [12]. Specifically, an RIS consists of a large number of reconfigurable passive components, each of which can cause the change of the amplitude and phase of the incident signal [13]. We can significantly enhance the link quality and cell coverage by appropriately adjusting the amplitude

- Part of this article was presented at the IEEE Global Communications Conference (GLOBECOM) 2022 [1].
- Y. Cheng is with the Alibaba-NTU Singapore Joint Research Institute, Nanyang Technological University, Singapore 639798. E-mail: yanyu.cheng@ntu.edu.sg.
- J. Lu, B. Lyu, and S. Zhu are with Alibaba Group, Hangzhou 311121, China. E-mail: gaolin.ljy@alibaba-inc.com; lubiao.lb@alibaba-inc.com; jianghe.zsm@alibaba-inc.com.
- D. Niyato and M. Xu are with the School of Computer Science and Engineering, Nanyang Technological University, Singapore 639798. E-mail: dniyato@ntu.edu.sg; minrui001@e.ntu.edu.sg.

reflection coefficients and phase shift variables [14]. Compared with traditional communication assistance technologies such as relays, RISs consume less energy resulting from passive reflection and can operate in full-duplex (FD) mode without self-interference [15]. On the other hand, NOMA can improve spectral efficiency by allocating multiple users to a single resource block. NOMA has been shown to outperform conventional orthogonal multiple access (OMA) in spectral efficiency, connection density, and user fairness [16]. However, it is not practical to assign many users to a single channel, due to high computational complexity. Therefore, user pairing is adopted to balance performance and computational complexity [12]. In particular, in a NOMA pair, the user with higher channel gain is called strong-signal user, while the user with lower channel gain is called weak-signal user.

1.1 Motivation and Contributions

To realize covert MEC in 6G, the application of covert communications to RIS-aided NOMA becomes crucial. The benefits of covert communications can be summarized as follows [17]:

- Covert communication provides a higher level of security than information-theoretic secrecy. With covert communications, the attacker does not know whether the transmission happens or not. As such, it cannot launch external attacks precisely.
- Compared with encryption, the performance of covert communications does not depend on the capabilities of the adversary. In other words, if the adversary has stronger information processing capability, the achievable security level will not be degraded.
- Covert communications can be implemented as an alternative or complementary solution to upper-layer security techniques such as steganography and encryption.

Although RIS-NOMA communications have been widely studied, covert RIS-NOMA has not been sufficiently investigated. The work in [9] studied covert RIS-NOMA. It realized covert transmission by leveraging the phase-shift uncertainty of RISs, where the link between the transmitter and the weaker-signal receiver is public and the link between the transmitter and the stronger-signal receiver is covert. Specifically, the **detection error probability** (DEP) of the warden was analyzed and its minimum value is used to optimize power allocation and maximize the covert data rate of the stronger-signal receiver. However, this design sacrifices the performance of the weaker-signal receiver, which can only achieve a predetermined minimum rate requirement. Also, it is applicable only to the case that the weaker-signal receiver adopt fix-rate transmission. Therefore, **we aim to improve both receivers' performance when applying covert communications to RIS-NOMA systems.** Furthermore, **we also introduce a friendly jammer to the system to increase the covertness, since it has been demonstrated effective to the covertness performance.** To be best of our knowledge, the jammer-aided covert RIS-NOMA has not been investigated. As the introduction of the jammer, the power allocation between the transmitter and jammer is necessary

to be addressed. To the end, the closed-form expressions for the DEP and ergodic data rates of both receivers are required, which can be used for analysis and optimization. As multiple channels are involved, the derivation of them is a challenging task. In summary, **this paper aims to design covert MEC systems with RIS-NOMA, analyze the corresponding performance, and optimize power allocation to improve system performance.** The contributions can be summarized as follows:

- We propose a novel covert MEC scheme with RIS-aided NOMA for security, where an RIS is used to expand cell coverage and a friendly jammer is applied to protect the transmission between the transmitter and the stronger-signal receiver.
- From the perspective of the worst-case for covert communications, we consider that the warden can optimally choose the detection threshold and realize minimum DEP. Correspondingly, we derive the closed-form expression for the average minimum DEP (AMDEP).
- Under the proposed scheme, the transmission between the transmitter and the stronger-signal receiver is covert and the transmission between the transmitter and the weaker-signal receiver is public. We analyze the performance of these two receivers and derive the closed-form expressions for ergodic covert rate and ergodic public rate.
- We design a reinforcement learning (RL)-based algorithm that optimizes the power allocation between the transmitter and the jammer to maximize the sum rate of two receivers while ensuring a high AMDEP, and investigate the effectiveness of the designed algorithm. Simulation results verifies the effectiveness of the designed scheme.

1.2 Organization

The remainder of this paper is organized as follows: In Section II, the related literature review is provided. In Section III, the model of the covert MEC with RIS-aided NOMA is described. Then, performance metrics and channel statistics required are presented in Section IV. Next, the performance of detection threshold and DEP at the warden is analyzed in Section V. Following that, in Section VI, the analysis of ergodic rates is conducted, and the power allocation optimization between the transmitter and jammer is realized by a designed RL algorithm. In Section VII, performance evaluation is conducted with numerical and simulation results. Lastly, this paper is concluded in Section VIII.

2 RELATED WORK

2.1 MEC and NOMA

There are many works focusing on MEC, including computation offloading, low latency, storage, energy efficiency [18]. For the computation task model, there are two computation-task models popularly used in existing literature on MEC [19], i.e., task model for binary offloading and task models for partial offloading. In the binary offloading model, tasks cannot be partitioned and must be executed locally on the mobile device as a whole or offloaded to the MEC server.

In contrast, in the partial offloading model, the input bits of the task are bitwise independent and can be divided into different groups to be executed by different entities (mobile devices or edge servers) [19].

Uplink NOMA is usually combined with binary offloading model, where multiple users offload their computation workloads simultaneously to an edge server [20]. In [20], the computation resource allocation and successive interference cancellation (SIC) order were optimized by minimizing latency. Downlink NOMA is suitable for combining with the partial offloading model, where a user can divide a whole computation task into multiple parts and simultaneously offload different parts to different edge servers with NOMA. It can effectively reduce the transmission delay of delivering computation workloads and reduce the overall delay of the execution on edge servers [21]. In [21], the optimal offloading strategy was obtained by minimizing the overall delay.

2.2 Reconfigurable Intelligent Surface

RISs are also known as passive holographic multiple-input multiple-output surfaces (HMIMOS) and have attracted a lot of research interests in both academia and industry [22]. For the application of RISs, accurate channel estimation is of high priority. In [23], a channel estimation framework based on parallel factor decomposition was proposed for uplink RIS-aided multi-user multiple-input single-output (MISO) systems. In [24], for energy-transfer MISO networks assisted by RISs, a channel estimation protocol was designed. To shorten the training sequences, a channel estimation framework was proposed for downlink RIS-aided multiple-input multiple-output (MIMO) networks in [25]. In [26], a three-phase pilot-based channel estimation scheme was proposed for MISO networks assisted by RISs to reduce the channel estimation time by utilizing the redundancy in the RIS-reflected channels of different users.

The superiority of an RIS was indicated as compared with a half-duplex (HD) decode-and-forward (DF) relay in [27]. In [28], the performance of a system aided by multiple RISs was evaluated, and it was revealed that the RIS-aided system outperforms the FD DF relay (FDR)-aided system when the number of RISs exceeds a certain value. Passive-beamforming design (i.e., phase-shift adjustment) for RISs is critical to system performance. In [29], multiple RISs were deployed in a single-input single-output (SISO) system, and the phase shifts of RISs were optimized by minimizing the outage probability. In [30], energy-efficient RIS-MIMO communications were studied by optimizing the transmit power allocation and the phase shifts of RISs. In [31], a hybrid beamforming scheme for multi-hop RIS-assisted terahertz communication networks was designed to improve coverage. The overhead that is required to estimate the CSI was taken into account the resource allocation for RIS-aided networks in [32]. Active and passive beamforming were jointly optimized for RIS-aided MISO systems in [33], [34] with different objectives.

2.3 RIS-Aided NOMA

Since both RISs and NOMA are candidate technologies for next-generation networks, which will be fundamental

technologies to MEC, the combination of RISs and NOMA has been widely studied. In [12], an RIS was utilized to improve the coverage by helping a cell-edge user, where this cell-edge user and a cell-center user form a NOMA pair. In [35], an RIS served multiple users that are in a NOMA group, where the RIS's parameters were designed for a prioritized user, and the performance of the prioritized user was analyzed. In [14], multiple RISs were deployed in NOMA systems, and two scenarios with and without direct links between the base station (BS) and users are considered for performance characterization. In [36] and [37], the beamforming vectors of the BS and RIS were optimized for RIS-NOMA systems. There can be a line-of-sight (LoS) link between a BS and an RIS since both BS and RIS are pre-deployed. In [38], the LoS BS-RIS-user link was considered in RIS-aided NOMA systems, and the active and passive beamforming was jointly optimized.

2.4 Covert Communications

RISs' phase shifts can be exploited to create uncertainty for covert communications [39]. In [40], it is demonstrated that the use of RIS can realize the perfect covertness even for a single-antenna transmitter. In [41], the covertness of RIS-aided systems was realized by utilizing transmission randomness and the uncertainty of RIS's phase shifts. In [42], the transmission power at the transmitter and the phase shifts at the RIS are jointly optimized by maximizing the covert data rate for both cases of instantaneous and partial channel state information (CSI) of the warden's link. In an RIS-aided system, the receiver can transmit jamming signals to confuse the warden, and the active and passive beamforming vectors are jointly optimized by maximizing the covert rate [43]. For the application of RISs, it is crucial to estimate accurate channel conditions of legitimate users. A channel acquisition protocol was designed for RIS-aided multi-user MISO networks in [24]. To reduce the channel estimation time, the authors proposed a three-phase pilot-based channel estimation scheme for RIS-aided MISO networks in [26]. The authors proposed a channel estimation framework to shorten the training sequences for downlink RIS-aided multiple-input multiple-output (MIMO) networks in [25]. The authors designed a message-passing based channel estimation algorithm for uplink RIS-aided MIMO networks in [44].

Since the security demand, covert communications have been gradually applied to NOMA. Under the NOMA scheme, the transmit power to the weaker-signal user is higher than that to the stronger-signal user. Therefore, the transmission between the BS and weaker-signal user is a natural shield for the transmission between the BS and stronger-signal user. In [45], a covert transmission between the BS and the stronger-signal user was realized by utilizing a public transmission between the BS and the weaker-signal user. Furthermore, the similar idea was applied for the uplink NOMA scenario in [46]. In [47], covert device-to-device (D2D)-based NOMA was investigated, where D2D transmission link is covert and the link between the BS and cellular user is public. In [48], covert NOMA-based vehicular communications were considered and implemented by exploiting friendly jamming.

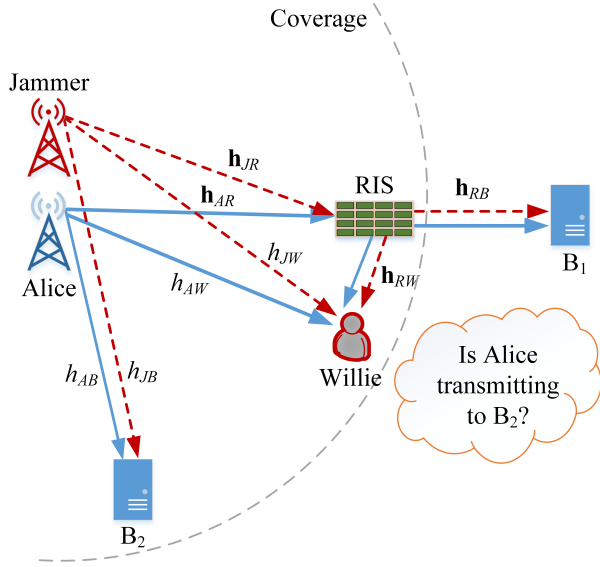


Fig. 1: The system model of covert MEC with RIS-assisted NOMA.

3 SYSTEM MODEL

The designed covert MEC model is to hide the existence of task offloading or computational result feedback between edge servers and users. Essentially, it is to hide the existence of information transmission between transmitters and receivers. Without loss of generality, we consider a system which consists of a legitimate transmitter (Alice), a pair of receivers (B_1 and B_2) forming a NOMA pair, an RIS, and a friendly jammer (Jammer) as shown in Fig. 1. In particular, the transmission of Alice- B_2 is covert, and the transmission of Alice- B_1 is public. A warden (Willie) aims to detect whether Alice is sending messages to B_2 . Specifically, B_2 is a cell-center receiver that can communicate with Alice directly, while B_1 is a cell-edge receiver. Since there is no direct link between Alice and B_1 due to long distance and blocking objects, an RIS is deployed to assist it in communications. Jammer is next to Alice and controlled by Alice to reduce the probability that the transmission between Alice and B_2 is successfully detected by Willie. Note that all nodes have a single antenna.

The RIS has N reflecting elements, and its reflection-coefficient matrix is denoted by $\Theta = \text{diag}(\beta_1 e^{j\theta_1}, \beta_2 e^{j\theta_2}, \dots, \beta_N e^{j\theta_N})$ ($j = \sqrt{-1}$), where $\beta_n \in [0, 1]$ is the amplitude-reflection coefficient and $\theta_n \in [0, 2\pi)$ is the phase-shift variable of the n th element that can be adjusted by the RIS ($n = 1, 2, \dots, N$). The signals reflected by the RIS twice or more times are ignored because of severe path loss [12], [15].

3.1 Channel Model

Quasi-static flat fading is considered for all channels. The fading coefficients between Alice/Jammer and Willie are denoted by h_{AW}/h_{JW} , respectively. The fading coefficients between Alice/Jammer and B_2 are denoted by h_{AB}/h_{JB} , respectively. The fading coefficient vectors between Alice/Jammer/ B_1 /Willie and RIS are denoted by $\mathbf{h}_{AR}/\mathbf{h}_{JR}/\mathbf{h}_{RB}/\mathbf{h}_{RW}$, respectively, and the space of these

vectors is $N \times 1$. All channels can be either LoS or NLoS, and we consider that all fading coefficients follow the Nakagami- m fading model with the fading parameters m_χ , where $\chi \in \{AR, JR, RB, RW, AB, JB, AW, JW\}$ indicates the same meaning as in fading coefficients [12]. In particular, it is NLoS for $m_\chi = 1$ and is LoS for $m_\chi > 1$. Moreover, all channels experience path loss with a path loss coefficient α_χ .

For the availability of CSI, we consider the following:

- Alice perfectly knows the instantaneous CSI of the links of Alice- B_2 and Alice-RIS- B_1 [15].
- Alice also perfectly knows the instantaneous CSI of the links of Jammer- B_2 and Jammer-RIS- B_1 , since Jammer is controlled by Alice [15].
- Alice only possesses the statistical CSI of Alice-Willie and RIS-Willie links, since Willie tries to hide its existence from legitimate systems, making it difficult for Alice to measure its instantaneous CSI [9].
- Willie possesses the perfect CSI of the Alice-Willie, Alice-RIS-Willie, Jammer-Willie, and Jammer-RIS-Willie links, which is the worst case for covert communications [9], [42].

In particular, several channel estimation schemes for RIS-assisted systems have been proposed to acquire the accurate CSI [23], [24], [25], [26].

3.2 Signal Model

Alice transmits the signal sequence $x_A(k) = \sqrt{\alpha_1 P_A} s_1(k) + \sqrt{\alpha_2 P_A} s_2(k)$, $k = 1, 2, \dots, K$, where P_A is the transmit power of Alice, $s_1(k)$ and $s_2(k)$ ($\mathbb{E}(|s_1(k)|^2) = \mathbb{E}(|s_2(k)|^2) = 1$) are the transmitted messages to B_1 and B_2 , respectively, and α_1 and α_2 are the power allocation coefficients for B_1 and B_2 , respectively ($\alpha_1 + \alpha_2 = 1$). Note that we assume the fixed power allocation between two receivers and set $\alpha_1 > \alpha_2$ for fairness. On the other hand, Jammer sends the interference signal sequence $x_J(k) = \sqrt{P_J} s_J(k)$, $k = 1, 2, \dots, K$, where P_J is the jamming power, and $s_J(k)$ ($\mathbb{E}(|s_J(k)|^2) = 1$) is the jamming message to confuse Willie. The jamming power P_J is a random variable that is uniformly distributed in $[0, \hat{P}_J]$, which is to create uncertainty [48]. Its probability density function (PDF) is given by

$$f_{P_J}(x) = \begin{cases} \frac{1}{\hat{P}_J}, & 0 \leq x \leq \hat{P}_J, \\ 0, & \text{otherwise.} \end{cases} \quad (1)$$

The received signals at B_1 and B_2 are given by

$$y_1(k) = (\mathbf{h}_{RB}^T \Theta \mathbf{h}_{AR} \sqrt{\mathcal{L}_1}) x_A(k) + (\mathbf{h}_{RB}^T \Theta \mathbf{h}_{JR} \sqrt{\mathcal{L}_2}) x_J(k) + n_1(k), \quad (2)$$

and

$$y_2(k) = h_{AB} \sqrt{\mathcal{L}_3} x_A(k) + h_{JB} \sqrt{\mathcal{L}_4} x_J(k) + n_2(k), \quad (3)$$

respectively, where $\sqrt{\mathcal{L}_1}$, $\sqrt{\mathcal{L}_2}$, $\sqrt{\mathcal{L}_3}$, and $\sqrt{\mathcal{L}_4}$ are path loss. Here, $\mathcal{L}_1 = L(d_{RB})L(d_{AR})$, $\mathcal{L}_2 = L(d_{RB})L(d_{JR})$, $\mathcal{L}_3 = L(d_{AB})$, $\mathcal{L}_4 = L(d_{JB})$, where $L(d_\chi) = d_\chi^{-\alpha_\chi}$, d_χ is the distance, α_χ is the path loss coefficient, and $\chi \in \{AR, JR, RB, RW, AB, JB, AW, JW\}$ [35], [49].

At B_1 , its message is detected directly by regarding B_2 's signal as interference, and the signal-to-interference-plus-noise ratio (SINR) is expressed as

$$\psi_1(k) = \frac{\alpha_1 P_A |\mathbf{h}_{RB}^T \mathbf{\Theta} \mathbf{h}_{AR}|^2 \mathcal{L}_1}{\alpha_2 P_A |\mathbf{h}_{RB}^T \mathbf{\Theta} \mathbf{h}_{AR}|^2 \mathcal{L}_1 + \varrho P_J |\mathbf{h}_{RB}^T \mathbf{\Theta} \mathbf{h}_{JR}|^2 \mathcal{L}_2 + \sigma_1^2}, \quad (4)$$

where $\varrho \in [0, 1]$ is the self-interference cancellation coefficient. At B_2 , the signal of B_1 is decoded first, and the corresponding SINR is given by

$$\psi_{2 \leftarrow 1}(k) = \frac{\alpha_1 P_A |h_{AB}|^2 \mathcal{L}_3}{\alpha_2 P_A |h_{AB}|^2 \mathcal{L}_3 + \varrho P_J |h_{JB}|^2 \mathcal{L}_4 + \sigma_2^2}. \quad (5)$$

The signal of B_2 is decoded after implementing the SIC, and the corresponding SINR is expressed as

$$\psi_2(k) = \frac{\alpha_2 P_A |h_{AB}|^2 \mathcal{L}_3}{\varrho P_J |h_{JB}|^2 \mathcal{L}_4 + \sigma_2^2}. \quad (6)$$

As an illegitimate warden, Willie aims to determine whether Alice is sending messages to B_2 based on the received signal sequence $y_W(k)$, $k = 1, 2, \dots, K$, via the Neyman-Pearson test [40], [41], [42], [43]. Consequently, Willie faces a binary detection problem: 1) the null hypothesis \mathcal{H}_0 which means that Alice is not transmitting to B_2 ; 2) the alternate hypothesis \mathcal{H}_1 indicating that Alice is transmitting to B_2 . The received signals observed by Willie under two hypotheses are as follows:

$$\begin{aligned} \mathcal{H}_0 : y_W(k) &= \left(h_{JW} \sqrt{\mathcal{L}_5} + \mathbf{h}_{RW}^T \mathbf{\Theta} \mathbf{h}_{JR} \sqrt{\mathcal{L}_6} \right) x_J(k) \\ &+ \left(h_{AW} \sqrt{\mathcal{L}_7} + \mathbf{h}_{RW}^T \mathbf{\Theta} \mathbf{h}_{AR} \sqrt{\mathcal{L}_8} \right) x_1(k) + n_W(k), \end{aligned} \quad (7)$$

$$\begin{aligned} \mathcal{H}_1 : y_W(k) &= \left(h_{JW} \sqrt{\mathcal{L}_5} + \mathbf{h}_{RW}^T \mathbf{\Theta} \mathbf{h}_{JR} \sqrt{\mathcal{L}_6} \right) x_J(k) \\ &+ \left(h_{AW} \sqrt{\mathcal{L}_7} + \mathbf{h}_{RW}^T \mathbf{\Theta} \mathbf{h}_{AR} \sqrt{\mathcal{L}_8} \right) x_A(k) + n_W(k), \end{aligned} \quad (8)$$

where $x_1(k) = \sqrt{\alpha_1 P_A} s_1(k)$, $\mathcal{L}_5 = L(d_{JW})$, $\mathcal{L}_6 = L(d_{RW})L(d_{JR})$, $\mathcal{L}_7 = L(d_{AW})$, and $\mathcal{L}_8 = L(d_{RW})L(d_{AR})$. It is noted that when Alice is not transmitting to B_2 , the power allocated to B_1 does not change. The reasons are as follows: 1) In practice, B_1 's demand for data rate does not change rapidly, and B_1 does not require more power when Alice is not transmitting to B_2 . 2) These two hypotheses are formed from the perspective of Willie. If Willie assumes that the power of Alice is all allocated to B_1 when Alice is not transmitting to B_2 , these will be no difference between \mathcal{H}_0 and \mathcal{H}_1 in terms of the received power at Willie, and Willie can only guess whether Alice is transmitting to B_2 or not. The same hypothesis setting can be found in [9], [45], [47].

Based on [7] and [8], Willie uses a radiometer for the binary detection. By monitoring the average received power at Willie, $P_W = \frac{1}{K} \sum_{k=1}^K |y_W(k)|^2$ the decision rule is as follows:

$$P_W \underset{\mathcal{D}_0}{\overset{\mathcal{D}_1}{\geq}} \tau, \quad (9)$$

where $\tau > 0$ is the detection threshold of Willie, \mathcal{D}_0 and \mathcal{D}_1 are the decisions in favor of \mathcal{H}_0 and \mathcal{H}_1 , respectively. We consider that Willie uses an infinite number of signal

samples for the binary detection, i.e., $K \rightarrow \infty$ [9]. As a result, the uncertainty of transmitted signals and received noises does not exist, and the average received power at Willie is given by

$$P_W = \begin{cases} \zeta_1 P_J + \zeta_2, & \mathcal{H}_0, \\ \zeta_1 P_J + \zeta_3, & \mathcal{H}_1, \end{cases} \quad (10)$$

where $\zeta_1 = \mathcal{L}_5 |h_{JW}|^2 + \mathcal{L}_6 |\mathbf{h}_{RW}^T \mathbf{\Theta} \mathbf{h}_{JR}|^2$, $\zeta_2 = \mathcal{L}_7 \alpha_1 P_A |h_{AW}|^2 + \mathcal{L}_8 \alpha_1 P_A |\mathbf{h}_{RW}^T \mathbf{\Theta} \mathbf{h}_{AR}|^2 + \sigma_W^2$, and $\zeta_3 = \mathcal{L}_7 P_A |h_{AW}|^2 + \mathcal{L}_8 P_A |\mathbf{h}_{RW}^T \mathbf{\Theta} \mathbf{h}_{AR}|^2 + \sigma_W^2$.

4 PERFORMANCE METRICS AND CHANNEL STATISTICS

In this section, we first illustrate performance metrics, and then present the channel statistics that are required to analyze performance.

4.1 Performance Metrics

In this paper, we mainly investigate two metrics to measure system performance, which are DEP and covert communication rate.

4.1.1 Detection Error Probability

The performance of Willie's hypothesis test can be characterized by DEP, and its definition is

$$\xi = \mathbb{P}_{FA} + \mathbb{P}_{MD}, \quad (11)$$

where $\mathbb{P}_{FA} = \mathbb{P}(\mathcal{D}_1 | \mathcal{H}_0)$ is the false alarm probability, $\mathbb{P}_{MD} = \mathbb{P}(\mathcal{D}_0 | \mathcal{H}_1)$ is the miss detection probability, and $\xi \in [0, 1]$. Specifically, $\xi = 0$ indicates that Willie can detect the covert transmission, while $\xi = 1$ reveals that Willie detects the covert transmission with a random guess.

4.1.2 Ergodic Covert and Public Rate

The transmission between the Alice and B_1 is public, and we define the corresponding data rate as public rate. The ergodic public rate of B_1 is given by

$$\bar{R}_1 = \mathbb{E}(B \log_2(1 + \psi_1)), \quad (12)$$

where B is the bandwidth, which is set to be 1 without loss of generality.

The message to B_2 is transmitted under covert communications, and the corresponding data rate is called covert rate. The ergodic covert rate of B_2 is given by

$$\bar{R}_2 = \mathbb{E}(B \log_2(1 + \psi_2)). \quad (13)$$

Remark 1. For the adaptive-rate transmission, the SINR at B_1 is $\min\{\psi_{2 \leftarrow 1}, \psi_1\}$. However, the path loss of B_1 is much larger than that of B_2 due to different distances to Alice. Hence, we have $\min\{\psi_{2 \leftarrow 1}, \psi_1\} \approx \psi_1$.

4.2 Channel Statistics

To analyze system performance, exact channel statistics are required.

4.2.1 Alice-B₁, Jammer-B₁, Alice-Willie, and Jammer-Willie Links

Since all channels experience Nakagami- m fading, the PDF and cumulative distribution function (CDF) of $|h_\varphi|^2$ ($\varphi \in \{AB, JB, AW, JW\}$) are given by

$$f_{|h_\varphi|^2}(x) = \frac{m_\varphi^{m_\varphi} x^{m_\varphi-1}}{\Gamma(m_\varphi)} e^{-m_\varphi x}, \quad (14)$$

and

$$F_{|h_\varphi|^2}(x) = \frac{\gamma(m_\varphi, m_\varphi x)}{\Gamma(m_\varphi)}, \quad (15)$$

for $x \geq 0$, respectively, where $\gamma(\cdot, \cdot)$ is the lower incomplete gamma function, and $\Gamma(\cdot)$ is the gamma function [12].

4.2.2 Alice-RIS-B₁ Link

The parameters of the RIS are adjusted by providing the best channel quality to B₁, i.e., by maximizing the channel gain of the Alice-RIS-B₁ link as follows:

$$|\mathbf{h}_{RB}^T \mathbf{\Theta} \mathbf{h}_{AR}| = \left| \sum_{n=1}^N \beta_n h_{RB,n} h_{AR,n} e^{j\theta_n} \right|, \quad (16)$$

where $h_{RB,n}$ and $h_{AR,n}$ are the n th element of \mathbf{h}_{RB} and \mathbf{h}_{AR} , respectively. The maximization of the channel gain can be realized by adjusting all phase-shift variables θ_n ($n = 1, 2, \dots, N$), i.e., setting the phases of all $h_{RB,n} h_{AR,n} e^{j\theta_n}$ to be the same. Hence, there is a generalized solution that is given by $\theta_n^* = \tilde{\theta} - \arg(h_{RB,n} h_{AR,n})$, where $\tilde{\theta}$ is an arbitrary constant in the range $[0, 2\pi)$. After using the optimal $\{\theta_n^*\}$, we have

$$|\mathbf{h}_{RB}^T \mathbf{\Theta} \mathbf{h}_{AR}|^2 = \beta^2 \left(\sum_{n=1}^N |h_{RB,n}| |h_{AR,n}| \right)^2, \quad (17)$$

where $\beta_n = \beta, \forall n$ without loss of generality.

The PDF of the equivalent channel gain after adopting the optimal $\{\theta_n^*\}$ is presented as follows: Denote that $|g_{ARB}|^2 = \frac{(\sum_{n=1}^N |h_{RB,n}| |h_{AR,n}|)^2}{N(1-\mu)}$, where $\mu = \frac{1}{m_{RB} m_{AR}} \left(\frac{\Gamma(m_{RB} + \frac{1}{2})}{\Gamma(m_{RB})} \right)^2 \left(\frac{\Gamma(m_{AR} + \frac{1}{2})}{\Gamma(m_{AR})} \right)^2$. When the number of reflecting elements N is large, $|g_{ARB}|^2$ tends to follow a noncentral chi-square distribution as $|g_{ARB}|^2 \sim \chi_1^2(\lambda)$, where $\lambda = \frac{N\mu}{1-\mu}$ [12]. Its PDF and CDF are given by

$$f_{|g_{ARB}|^2}(x) = e^{-\frac{x+\lambda}{2}} \sum_{i=0}^{\infty} \frac{\lambda^i x^{i-\frac{1}{2}}}{i! 2^{i+\frac{1}{2}} \Gamma(i+\frac{1}{2})}, \quad (18)$$

and

$$F_{|g_{ARB}|^2}(x) = e^{-\frac{x}{2}} \sum_{i=0}^{\infty} \frac{\lambda^i \gamma(i+\frac{1}{2}, \frac{x}{2})}{i! 2^i \Gamma(i+\frac{1}{2})}, \quad (19)$$

for $x \geq 0$, respectively.

4.2.3 Alice-RIS-Willie, Jammer-RIS-B₁, and Jammer-RIS-Willie Links

For these links, the phase shifts of the RIS can be regarded as random, since the parameters of RIS are designed for the Alice-RIS-B₁ link [9], [49]. Denote that $g_{ARW} = \frac{\mathbf{h}_{RW}^T \mathbf{\Theta} \mathbf{h}_{AR}}{\beta} = \sum_{n=1}^N h_{RW,n} h_{AR,n} e^{j\theta_n^*}$, $g_{JRB} = \frac{\mathbf{h}_{RB}^T \mathbf{\Theta} \mathbf{h}_{JR}}{\beta} =$

$\sum_{n=1}^N h_{RB,n} h_{JR,n} e^{j\theta_n^*}$, and $g_{JRW} = \frac{\mathbf{h}_{RW}^T \mathbf{\Theta} \mathbf{h}_{JR}}{\beta} = \sum_{n=1}^N h_{RW,n} h_{JR,n} e^{j\theta_n^*}$. With [9], [49], when $\{\theta_n\}$ is random and N is sufficiently large, g_ϕ ($\phi \in \{ARW, JRB, JRW\}$) tends to a complex Gaussian random variable with mean zero and variance N , i.e., $g_\phi \sim \mathcal{CN}(0, N)$. Consequently, the PDF and CDF of $|g_\phi|^2$ ($\phi \in \{ARW, JRB, JRW\}$) are given by

$$f_{|g_\phi|^2}(x) = \frac{1}{N} e^{-\frac{x}{N}}, \quad (20)$$

and

$$F_{|g_\phi|^2}(x) = 1 - e^{-\frac{x}{N}}, \quad (21)$$

for $x \geq 0$, respectively.

5 PERFORMANCE ANALYSIS FOR DETECTION ERROR PROBABILITY

In this section, we analyze the performance of DEP. Specifically, the DEPs for the fixed detection threshold and the optimal detection threshold are derived.

5.1 Fixed Detection Threshold

With a threshold τ , the DEP of Willie is presented in the theorem below.

Theorem 1. *Given a detection threshold τ , there are two cases for the DEP as follows:*

Case 1: When $\tau_2 \leq \tau_3$, the DEP of Willie is given by

$$\xi = \begin{cases} 1, & \tau < \tau_1, \\ 1 - \frac{\tau - \zeta_2}{\zeta_1 \hat{P}_J}, & \tau_1 \leq \tau < \tau_2, \\ 0, & \tau_2 \leq \tau < \tau_3, \\ \frac{\tau - \zeta_3}{\zeta_1 \hat{P}_J}, & \tau_3 \leq \tau < \tau_4, \\ 1, & \tau \geq \tau_4, \end{cases} \quad (22)$$

where $\tau_1 = \zeta_2$, $\tau_2 = \zeta_1 \hat{P}_J + \zeta_2$, $\tau_3 = \zeta_3$, and $\tau_4 = \zeta_1 \hat{P}_J + \zeta_3$.

Case 2: When $\tau_2 > \tau_3$, the DEP of Willie is given by

$$\xi = \begin{cases} 1, & \tau < \tau_1, \\ 1 - \frac{\tau - \zeta_2}{\zeta_1 \hat{P}_J}, & \tau_1 \leq \tau < \tau_3, \\ 1 - \frac{\zeta_3 - \zeta_2}{\zeta_1 \hat{P}_J}, & \tau_3 \leq \tau < \tau_2, \\ \frac{\tau - \zeta_3}{\zeta_1 \hat{P}_J}, & \tau_2 \leq \tau < \tau_4, \\ 1, & \tau \geq \tau_4. \end{cases} \quad (23)$$

Proof. Based on (9) and (10), we can obtain the false alarm probability and miss detection probability as

$$\mathbb{P}_{FA} = \Pr(\zeta_1 P_J + \zeta_2 > \tau), \quad (24)$$

and

$$\mathbb{P}_{MD} = \Pr(\zeta_1 P_J + \zeta_3 \leq \tau), \quad (25)$$

respectively.

First, the false alarm probability can be derived as

$$\begin{aligned} \mathbb{P}_{FA} &= P_r \left(P_J > \frac{\tau - \zeta_2}{\zeta_1} \right) \\ &= \begin{cases} 1, & \tau < \tau_1, \\ 1 - \frac{\tau - \zeta_2}{\zeta_1 \hat{P}_J}, & \tau_1 \leq \tau < \tau_2, \\ 0, & \tau \geq \tau_2. \end{cases} \end{aligned} \quad (26)$$

Then, the miss detection probability can be derived as

$$\begin{aligned} \mathbb{P}_{MD} &= P_r \left(P_J \leq \frac{\tau - \zeta_3}{\zeta_1} \right) \\ &= \begin{cases} 0, & \tau < \tau_3, \\ \frac{\tau - \zeta_3}{\zeta_1 \hat{P}_J}, & \tau_3 \leq \tau < \tau_4, \\ 1, & \tau \geq \tau_4. \end{cases} \end{aligned} \quad (27)$$

Since $\xi = \mathbb{P}_{FA} + \mathbb{P}_{MD}$, we can derive the DEP of Willie, and this completes the proof. ■

5.2 Optimal Detection Threshold and Minimum Detection Error Probability

It is worth noting that the aforementioned DEP is derived based on a fixed detection threshold τ . However, Willie can adjust the threshold to achieve the minimum DEP, which is the worst case for covert communications. It is necessary to analyze the performance for the worst case. The optimal detection threshold τ^* is presented in the following lemma.

Lemma 1. For Willie, the optimal detection threshold that minimizes the detection probability is given by

$$\tau^* \in \begin{cases} [\tau_2, \tau_3], & \tau_2 \leq \tau_3, \\ [\tau_3, \tau_2], & \tau_2 > \tau_3. \end{cases} \quad (28)$$

Proof. For the first case ($\tau_2 \leq \tau_3$), it is obvious that the minimum DEP is 0, which locates in the interval $[\tau_2, \tau_3]$.

For the second case ($\tau_2 > \tau_3$), the DEP is 1 for $\tau \in [0, \tau_1] \cup [\tau_4, \infty]$. The DEP monotonically decreases and increases for $\tau \in [\tau_1, \tau_2]$ and $[\tau_3, \tau_4]$, respectively. Hence, the constant value for $\tau \in [\tau_2, \tau_3]$ is the minimum DEP.

Since the DEP is continuous, by summarizing the results, we can complete the proof. ■

By adopting the optimal detection threshold, Willie can realize the minimum DEP as shown in the following theorem.

Theorem 2. The minimum DEP of Willie is given by

$$\xi^* = \begin{cases} 0, & \tau_2 \leq \tau_3, \\ 1 - \frac{\zeta_3 - \zeta_2}{\zeta_1 \hat{P}_J}, & \tau_2 > \tau_3. \end{cases} \quad (29)$$

Proof. Based on Theorem 1 and Lemma 1, it is easy to obtain this theorem. ■

5.3 Average Minimum Detection Error Probability

Based on the statistical CSI of all channels, we can derive the AMDEP of Willie. The average minimum DEP can be derived by

$$\begin{aligned} \xi_a^* &= P_r(\tau_2 \leq \tau_3) \mathbb{E}(\xi^* | \tau_2 \leq \tau_3) \\ &\quad + P_r(\tau_2 > \tau_3) \mathbb{E}(\xi^* | \tau_2 > \tau_3) \\ &= P_r(\tau_2 > \tau_3) \mathbb{E}(\xi^* | \tau_2 > \tau_3). \end{aligned} \quad (30)$$

Hence, $P_r(\tau_2 > \tau_3)$ and $\mathbb{E}(\xi^* | \tau_2 > \tau_3)$ are required, which are presented in the following lemmas.

Lemma 2. The probability of $\tau_2 > \tau_3$ is given by

$$P_r(\tau_2 > \tau_3) \approx \Xi_1 \Xi_3 + \Xi_2 (1 - \Xi_3), \quad (31)$$

where Ξ_1 , Ξ_2 , and Ξ_3 are defined as follows:

$$\begin{aligned} \Xi_1 &= \frac{\eta_4 \eta_6^{m_{JW}} \Gamma(m_{AW} + m_{JW})}{m_{JW} (\eta_5 + \eta_6)^{m_{AW} + m_{JW}}} \\ &\quad \times {}_2F_1 \left(1, m_{AW} + m_{JW}; m_{JW} + 1; \frac{\eta_6}{\eta_5 + \eta_6} \right), \end{aligned} \quad (32)$$

$$\begin{aligned} \Xi_2 &= \frac{\eta_7 \Gamma(m_{AW})}{\eta_8^{m_{AW}}} - \frac{\eta_9 \eta_{11}^{m_{JW}} \Gamma(m_{AW} + m_{JW})}{m_{AW} (\eta_{10} + \eta_{11})^{m_{AW} + m_{JW}}} \\ &\quad \times {}_2F_1 \left(1, m_{AW} + m_{JW}; m_{AW} + 1; \frac{\eta_{10}}{\eta_{10} + \eta_{11}} \right), \end{aligned} \quad (33)$$

and

$$\begin{aligned} \Xi_3 &= \frac{\eta_{12} \eta_{13}^{m_{JW}} \Gamma(m_{AW} + m_{JW})}{m_{JW} (\eta_{13} + m_{AW})^{m_{AW} + m_{JW}}} \\ &\quad \times {}_2F_1 \left(1, m_{AW} + m_{JW}; m_{JW} + 1; \frac{\eta_{13}}{\eta_{13} + m_{AW}} \right), \end{aligned} \quad (34)$$

with $\eta_1 = \frac{\mathcal{L}_6 \hat{P}_J}{\mathcal{L}_8 \alpha_2 P_A}$, $\eta_2 = \frac{\mathcal{L}_5 \hat{P}_J}{\mathcal{L}_8 \alpha_2 P_A \beta^2}$, $\eta_3 = \frac{\mathcal{L}_7}{\mathcal{L}_8 \beta^2}$, $\eta_4 = \frac{\eta_1 m_{JW} m_{AW}}{(\eta_1 + 1) \Gamma(m_{JW}) \Gamma(m_{AW})} \left(m_{JW} - \frac{\eta_2}{N \eta_1} \right)^{-m_{JW}}$, $\eta_5 = m_{AW} + \frac{\eta_3}{N \eta_1}$, $\eta_6 = \frac{\eta_3 m_{JW}}{\eta_2} - \frac{\eta_3}{N \eta_1}$, $\eta_7 = \frac{m_{AW}}{\Gamma(m_{AW})}$, $\eta_8 = \frac{\eta_3}{\eta_2 N} + m_{AW}$, $\eta_9 = \frac{m_{JW} m_{AW}}{(\eta_1 + 1) \Gamma(m_{JW}) \Gamma(m_{AW})} \left(\frac{\eta_2}{N} + m_{JW} \right)^{-m_{JW}}$, $\eta_{10} = m_{AW} - \frac{\eta_3}{N}$, $\eta_{11} = \frac{\eta_3}{N} + \frac{\eta_3 m_{JW}}{\eta_2}$, $\eta_{12} = \frac{m_{AW}}{\Gamma(m_{AW}) \Gamma(m_{JW})}$, $\eta_{13} = \frac{m_{JW} \eta_3}{\eta_2}$, and ${}_2F_1(\cdot, \cdot; \cdot; \cdot)$ being Gauss hypergeometric function.

Proof. We can derive $P_r(\tau_2 > \tau_3)$ by (35). There are three terms required to derive, i.e., Ξ_1 , Ξ_3 , and Ξ_2 . First, according to (21), we can derive $\mathcal{J}_1 = 1 - e^{\frac{\eta_3 z - \eta_1 x - \eta_2 y}{N}}$. Next, based on (20), we have $\mathcal{J}_2 = \frac{\eta_1}{\eta_1 + 1} e^{\frac{\eta_2 y - \eta_3 z}{N \eta_1}}$. Then, according to (14), we can obtain $\mathcal{J}_3 = \frac{\eta_1 m_{JW}}{(\eta_1 + 1) \Gamma(m_{JW})} e^{-\frac{\eta_3 z}{N \eta_1}} \left(m_{JW} - \frac{\eta_2}{N \eta_1} \right)^{-m_{JW}} \gamma(m_{JW}, \eta_6 z)$, by referring to [50, eq. (3.381.1)]. Finally, we can derive Ξ_1 by

$$\Xi_1 = \eta_4 \int_0^\infty z^{m_{AW} - 1} e^{-\eta_5 z} \gamma(m_{JW}, \eta_6 z) dz. \quad (36)$$

By referring to [50, eq. (6.455.2)], we can derive Ξ_1 as (32).

The derivation of Ξ_2 is similar to that of Ξ_1 . Since \mathcal{J}_1 has been derived, we can directly derive $\mathcal{J}_2' = 1 - \frac{1}{\eta_1 + 1} e^{\frac{\eta_3 z - \eta_2 y}{N}}$. Then, we can derive $\mathcal{J}_3' = e^{-\frac{\eta_3 z}{N \eta_1}} -$

$$\begin{aligned}
 P_r(\tau_2 > \tau_3) &= P_r(\zeta_1 \hat{P}_J + \zeta_2 > \zeta_3) \\
 &= \underbrace{\int_0^\infty \int_0^{\frac{\eta_3 z}{\eta_2}} \underbrace{\int_{\frac{\eta_3 z - \eta_2 y}{\eta_1}}^\infty \underbrace{\int_0^{\eta_1 x + \eta_2 y - \eta_3 z} f_{|g_{ARW}|^2}(w) dw}_{\mathcal{J}_1} f_{|g_{JRW}|^2}(x) dx}_{\mathcal{J}_2} f_{|h_{JW}|^2}(y) dy}_{\mathcal{J}_3} f_{|h_{AW}|^2}(z) dz}_{\Xi_1} P_r(\eta_2 |h_{JW}|^2 \leq \eta_3 |h_{AW}|^2) \\
 &\quad + \underbrace{\int_0^\infty \int_{\frac{\eta_3 z}{\eta_2}}^\infty \int_0^\infty \underbrace{\int_0^{\eta_1 x + \eta_2 y - \eta_3 z} f_{|g_{ARW}|^2}(w) dw}_{\mathcal{J}_1} f_{|g_{JRW}|^2}(x) dx}_{\mathcal{J}_2'} f_{|h_{JW}|^2}(y) dy}_{\mathcal{J}_3'} f_{|h_{AW}|^2}(z) dz}_{\Xi_2} P_r(\eta_2 |h_{JW}|^2 > \eta_3 |h_{AW}|^2).
 \end{aligned} \tag{35}$$

$\frac{m_{JW}^{m_{JW}}}{(\eta_1 + 1)\Gamma(m_{JW})} e^{\frac{\eta_3 z}{N}} (\frac{\eta_2}{N} + m_{JW})^{-m_{JW}} \Gamma(m_{JW}, \eta_{11} z)$, by referring to [50, eq. (3.381.3)]. Finally, we can derive Ξ_2 by

$$\begin{aligned}
 \Xi_2 &= \eta_7 \int_0^\infty z^{m_{AW}-1} e^{-\eta_8 z} dz \\
 &\quad - \eta_9 \int_0^\infty z^{m_{AW}-1} e^{-\eta_{10} z} \Gamma(m_{JW}, \eta_{11} z) dz.
 \end{aligned} \tag{37}$$

By referring to [50, eq. (3.326.2) and eq. (6.455.1)], we can derive Ξ_2 as (33).

For Ξ_3 , it can be derived as

$$\begin{aligned}
 \Xi_3 &= \int_0^\infty \int_0^{\frac{\eta_3 z}{\eta_2}} f_{|h_{JW}|^2}(y) dy f_{|h_{AW}|^2}(z) dz \\
 &= \eta_{12} \int_0^\infty z^{m_{AW}-1} e^{-m_{AW} z} \gamma(m_{JW}, \eta_{13} z) dz.
 \end{aligned} \tag{38}$$

With the help of [50, eq. (6.455.2)], we can derive Ξ_3 as (34). This completes the proof. ■

Lemma 3. The conditional expectation value of ξ_a^* is given by

$$\mathbb{E}(\xi^* | \tau_2 > \tau_3) \approx \frac{1}{2} \sum_{l=1}^{u_1} \omega_{1,l} \Phi_1(b_l), \tag{39}$$

where u_1 is the number of nodes for the Chebyshev-Gauss quadrature, $\omega_{1,l} = \frac{\pi}{u_1}$ is the weight, $b_l = \cos\left(\frac{2l-1}{2u_1}\pi\right)$, and

$$\Phi_1(b) = \Omega\left(\frac{b+1}{2}\right) \sqrt{1-b^2}, \tag{40}$$

with

$$\Omega(a) = \Delta_1 \Delta_3 + \Delta_2 (1 - \Delta_3). \tag{41}$$

The definitions of Δ_1 , Δ_2 , and Δ_3 are as follows:

$$\begin{aligned}
 \Delta_1 &= \frac{\nu_4 \nu_6^{m_{JW}} \Gamma(m_{AW} + m_{JW})}{m_{JW} (\nu_5 + \nu_6)^{m_{AW} + m_{JW}}} \\
 &\quad \times {}_2F_1\left(1, m_{AW} + m_{JW}; m_{JW} + 1; \frac{\nu_6}{\nu_5 + \nu_6}\right),
 \end{aligned} \tag{42}$$

$$\begin{aligned}
 \Delta_2 &= \frac{\nu_7 \Gamma(m_{AW})}{\nu_8^{m_{AW}}} - \frac{\nu_9 \nu_{11}^{m_{JW}} \Gamma(m_{AW} + m_{JW})}{m_{AW} (\nu_{10} + \nu_{11})^{m_{AW} + m_{JW}}} \\
 &\quad \times {}_2F_1\left(1, m_{AW} + m_{JW}; m_{AW} + 1; \frac{\nu_{10}}{\nu_{10} + \nu_{11}}\right),
 \end{aligned} \tag{43}$$

$$\begin{aligned}
 \Delta_3 &= \frac{\nu_{12} \nu_{13}^{m_{JW}} \Gamma(m_{AW} + m_{JW})}{m_{JW} (\nu_{13} + m_{AW})^{m_{AW} + m_{JW}}} \\
 &\quad \times {}_2F_1\left(1, m_{AW} + m_{JW}; m_{JW} + 1; \frac{\nu_{13}}{\nu_{13} + m_{AW}}\right),
 \end{aligned} \tag{44}$$

where $\nu_1 = \frac{\mathcal{L}_6 \hat{P}_J}{\mathcal{L}_8 \alpha_2 P_A} a$, $\nu_2 = \frac{\mathcal{L}_5 \hat{P}_J}{\mathcal{L}_8 \alpha_2 P_A \beta^2} a$, $\nu_3 = \frac{\mathcal{L}_7}{\mathcal{L}_8 \beta^2}$, $\nu_4 = \frac{\nu_1 m_{JW}^{m_{JW}} m_{AW}^{m_{AW}}}{(\nu_1 + 1) \Gamma(m_{JW}) \Gamma(m_{AW})} \left(m_{JW} - \frac{\nu_2}{N \nu_1}\right)^{-m_{JW}}$, $\nu_5 = m_{AW} + \frac{\nu_3}{N \nu_1}$, $\nu_6 = \frac{\nu_3 m_{JW}}{N \nu_1} - \frac{\nu_3}{N \nu_1}$, $\nu_7 = \frac{m_{AW}^{m_{AW}}}{\Gamma(m_{AW})}$, $\nu_8 = \frac{\nu_3}{\nu_2 N} + m_{AW}$, $\nu_9 = \frac{m_{JW}^{m_{JW}} m_{AW}^{m_{AW}}}{(\nu_1 + 1) \Gamma(m_{JW}) \Gamma(m_{AW})} \left(\frac{\nu_2}{N} + m_{JW}\right)^{-m_{JW}}$, $\nu_{10} = m_{AW} - \frac{\nu_3}{N}$, $\nu_{11} = \frac{\nu_3}{N} + \frac{\nu_3 m_{JW}}{\nu_2}$, $\nu_{12} = \frac{m_{AW}^{m_{AW}}}{\Gamma(m_{AW}) \Gamma(m_{JW})}$, and $\nu_{13} = \frac{m_{JW} \nu_3}{\nu_2}$.

Proof. We can derive $\mathbb{E}(\xi^* | \tau_2 > \tau_3)$ as

$$\mathbb{E}(\xi^* | \tau_2 > \tau_3) = 1 - \mathbb{E}\left(\frac{\zeta_3 - \zeta_2}{\zeta_1 \hat{P}_J} \middle| \zeta_3 - \zeta_2 < \zeta_1 \hat{P}_J\right). \tag{45}$$

Define that

$$A = \frac{\zeta_3 - \zeta_2}{\zeta_1 \hat{P}_J} = \frac{\mathcal{L}_7 \alpha_2 P_A |h_{AW}|^2 + \mathcal{L}_8 \alpha_2 P_A \beta^2 |g_{ARW}|^2}{\mathcal{L}_5 \hat{P}_J |h_{JW}|^2 + \mathcal{L}_6 \beta^2 \hat{P}_J |g_{JRW}|^2}. \tag{46}$$

The conditional CDF of A is given by

$$F_{A|\zeta_3 - \zeta_2 < \zeta_1 \hat{P}_J}(a) = P_r\left(\frac{\zeta_3 - \zeta_2}{\zeta_1 \hat{P}_J} \leq a \middle| \frac{\zeta_3 - \zeta_2}{\zeta_1 \hat{P}_J} < 1\right). \tag{47}$$

It is obvious that $F_{A|\zeta_3 - \zeta_2 < \zeta_1 \hat{P}_J}(a) = 1$ for $a \geq 1$. When $a < 1$, we have

$$\begin{aligned}
 F_{A|\zeta_3 - \zeta_2 < \zeta_1 \hat{P}_J}(a) &= P_r\left(\frac{\zeta_3 - \zeta_2}{\zeta_1 \hat{P}_J} \leq a\right) \\
 &= \underbrace{\Delta_1 \Delta_3 + \Delta_2 (1 - \Delta_3)}_{\Omega(a)},
 \end{aligned} \tag{48}$$

by referring to the calculation of (35). Therefore, we have

$$F_{A|\zeta_3-\zeta_2<\zeta_1\hat{P}_J}(a) = \begin{cases} \Omega(a), & a < 1, \\ 1, & a \geq 1. \end{cases} \quad (49)$$

Based on the conditional CDF of A , the conditional expectation of A can be derived as

$$\begin{aligned} \mathbb{E}(A|\zeta_3-\zeta_2<\zeta_1\hat{P}_J) &= 1 - \int_0^1 \Omega(a) da \\ &\stackrel{b=2a-1}{=} 1 - \frac{1}{2} \underbrace{\int_{-1}^1 \Omega\left(\frac{b+1}{2}\right) db}_{\mathcal{J}_4}. \end{aligned} \quad (50)$$

Next, by using the Chebyshev-Gauss quadrature, we can approximate \mathcal{J}_4 as $\mathcal{J}_4 \approx \sum_{l=1}^{u_1} \omega_{1,l} \Phi_1(b_l)$. Finally, we can derive $\mathbb{E}(\xi_a^*|\tau_2 > \tau_3)$ as (39). This completes the proof. ■

Based on Lemmas 2 and 3, the AMDEP of Willie is obtained as shown in the following theorem.

Theorem 3. *The AMDEP of Willie can be approximated as*

$$\xi_a^* \approx (\Xi_1 \Xi_3 + \Xi_2(1 - \Xi_3)) \left(\frac{1}{2} \sum_{l=1}^{u_1} \omega_{1,l} \Phi_1(b_l) \right). \quad (51)$$

6 PERFORMANCE ANALYSIS FOR ERGODIC RATES AND POWER ALLOCATION

In this section, we analyze the performance on ergodic covert and public rates. First, the scenario of fixed power allocation is analyzed. Following that, the scenario of adaptive power allocation is considered. Meanwhile, the optimal solution for power allocation is derived by a designed RL-based algorithm.

6.1 Fixed Power Allocation

Given a transmit power and a jamming power, the ergodic public rate of B_1 and the ergodic covert rate of B_2 are presented in the following theorem.

Theorem 4. *Given a P_A and \hat{P}_J , the ergodic public rate of B_1 is given by*

$$\bar{R}_1 = \log_2(1 + \tilde{\alpha}) - \frac{e^{-\frac{\lambda}{2}}}{\ln(2)} \sum_{i=0}^{\infty} \frac{\lambda^i}{i! 2^i \Gamma(i + \frac{1}{2})} \sum_{l=1}^{u_2} \omega_{2,l} \Phi_2(t_l), \quad (52)$$

where $\tilde{\alpha} = \frac{\alpha_1}{\alpha_2}$, u_2 is the number of nodes for the Chebyshev-Gauss quadrature, $\omega_{2,l} = \frac{\pi}{u_2}$ is the weight, $t_l = \cos\left(\frac{(2l-1)\pi}{2u_2}\right)$, $\varpi_1 = \alpha_1 N P_A (1 - \mu) \beta^2 \mathcal{L}_1$, $\varpi_2 = \alpha_2 N P_A (1 - \mu) \beta^2 \mathcal{L}_1$, and

$$\Phi_2(t) = \gamma\left(i + \frac{1}{2}, \frac{\sigma_1^2 \tilde{\alpha}(t+1)}{4\varpi_1 - 2\varpi_2 \tilde{\alpha}(t+1)}\right) \frac{\tilde{\alpha} \sqrt{1-t^2}}{2 + \tilde{\alpha}(t+1)}. \quad (53)$$

The ergodic covert rate of B_2 is given by

$$\bar{R}_2 = \frac{m_{AB}^{m_{AB}}}{\Gamma(m_{AB})} \sum_{l=1}^{u_3} \omega_{3,l} \Phi_3(x_l). \quad (54)$$

where u_3 is the number of nodes for the Gauss-Laguerre quadrature, $x_{3,l}$ is the l th root of Laguerre polynomial $L_{u_3}(x)$, $\omega_{3,l} = \frac{x_{3,l}}{(u_3+1)^2 (L_{u_3+1}(x_{3,l}))^2}$ is the weight, $\varpi_3 = \frac{\alpha_2 P_A \mathcal{L}_3}{\sigma_2^2}$, and

$$\Phi_3(x) = \log_2(1 + \varpi_3 x) x^{m_{AB}-1} e^{-(m_{AB}-1)x}. \quad (55)$$

Proof. We first analyze the ergodic public rate of B_1 . Since Jammer is friendly and controlled by Alice, we can assume that the interference can be perfectly eliminated, i.e., $\varrho = 0$, and the ergodic rate of B_1 can be expressed as

$$\bar{R}_1 = \mathbb{E} \left(\log_2 \left(1 + \frac{\varpi_1 |g_{ARB}|^2}{\varpi_2 |g_{ARB}|^2 + \sigma_1^2} \right) \right). \quad (56)$$

Denote that $Z = \frac{\varpi_1 |g_{ARB}|^2}{\varpi_2 |g_{ARB}|^2 + \sigma_1^2}$, and it is obvious that $0 \leq Z \leq \tilde{\alpha} = \frac{\varpi_1}{\varpi_2}$. Thus, the CDF of Z can be derived as

$$F_Z(z) = e^{-\frac{\lambda}{2}} \sum_{i=0}^{\infty} \frac{\lambda^i \gamma\left(i + \frac{1}{2}, \frac{\sigma_1^2 z}{2\varpi_1 - 2\varpi_2 z}\right)}{i! 2^i \Gamma(i + \frac{1}{2})}. \quad (57)$$

The ergodic public rate of B_1 can be derived by

$$\begin{aligned} R_1 &= - \int_0^{\tilde{\alpha}} \log_2(1+z) d(1 - F_Z(z)) \\ &= \frac{1}{\ln(2)} \int_0^{\tilde{\alpha}} \frac{1 - F_Z(z)}{1+z} dz \\ &= \log_2(1 + \tilde{\alpha}) - \frac{e^{-\frac{\lambda}{2}}}{\ln(2)} \sum_{i=0}^{\infty} \frac{\lambda^i}{i! 2^i \Gamma(i + \frac{1}{2})} \\ &\quad \times \underbrace{\int_0^{\tilde{\alpha}} \frac{\gamma\left(i + \frac{1}{2}, \frac{\sigma_1^2 z}{2\varpi_1 - 2\varpi_2 z}\right)}{1+z} dz}_{\mathcal{J}_5}. \end{aligned} \quad (58)$$

By denoting that $t = \frac{2z}{\tilde{\alpha}} - 1$ and using the Chebyshev-Gauss quadrature, we can approximate \mathcal{J}_5 as

$$\mathcal{J}_5 = \int_{-1}^1 \frac{\tilde{\alpha} \gamma\left(i + \frac{1}{2}, \frac{\sigma_1^2 \tilde{\alpha}(t+1)}{4\varpi_1 - 2\varpi_2 \tilde{\alpha}(t+1)}\right)}{2 + \tilde{\alpha}(t+1)} dt \simeq \sum_{l=1}^{u_2} \omega_{2,l} \Phi_2(t_l). \quad (59)$$

The ergodic covert rate of B_2 can be expressed as

$$\begin{aligned} \bar{R}_2 &= \mathbb{E}(\log_2(1 + \varpi_3 |h_{AB}|^2)) \\ &= \frac{m_{AB}^{m_{AB}}}{\Gamma(m_{AB})} \underbrace{\int_0^{\infty} \log_2(1 + \varpi_3 x) x^{m_{AB}-1} e^{-m_{AB}x} dx}_{\mathcal{J}_6}. \end{aligned} \quad (60)$$

By applying Gauss-Laguerre quadrature, we have $\mathcal{J}_6 = \sum_{l=1}^{u_3} \omega_{3,l} \Phi_3(x_l)$. This completes the proof. ■

As Alice's transmit power increases, the ergodic public rate of B_1 converges to a value, which is given in the following corollary.

Corollary 1. *When $P_A \rightarrow \infty$, the converged value of B_1 's ergodic public rate is expressed as*

$$\bar{R}_1^\infty = \log_2(1 + \tilde{\alpha}). \quad (61)$$

6.2 Optimization Problem Formulation of Power Allocation

To improve the system performance, we aim to maximize the sum rate of B_1 and B_2 by optimizing power allocation between the transmit power of Alice (P_A) and jamming

power's bound (\hat{P}_J). Accordingly, we can formulate the optimization problem as

$$\begin{aligned} & \text{maximize} \quad \bar{R}_1 + \bar{R}_2, \\ & P_A, \hat{P}_J \end{aligned} \quad (62a)$$

$$\text{subject to} \quad P_A + \hat{P}_J \leq P_{max}, \quad (62b)$$

$$\xi_a^* \geq 1 - \Lambda, \quad (62c)$$

where P_{max} is the total power limit. Specifically, (62a) is to maximize the sum rate of B_1 and B_2 , which is the summation of (52) and (54), (62b) contains the transmit power constraint, and (62c) is the covert constraint with Λ being a predefined factor to specify a certain covertness, where ξ_a^* is given by (51).

Since both the ergodic public rate of B_1 and the ergodic covert rate of B_2 increase with P_A , the maximum objective value of (62a) is achieved only when the equality in (62b) holds, i.e., $P_A + \hat{P}_J = P_{max}$. As such, we can simply (62) as follows:

$$\begin{aligned} & \text{maximize}_{\kappa} \quad \bar{R}_1 + \bar{R}_2, \\ & \text{subject to} \quad 0 \leq \kappa \leq 1, \end{aligned} \quad (63a)$$

$$\xi_a^* \geq 1 - \Lambda, \quad (63c)$$

where $\kappa = P_A/P_{max} = 1 - \hat{P}_J/P_{max}$ is the power allocation coefficient.

6.3 Methodology

The closed-form expressions for B_1 's ergodic public rate and B_2 's ergodic covert rate are complicated, and thus, it is non-trivial to directly obtain the optimal solution under constraints. Moreover, some parameters required for the optimization problem are not known in advance, and they have to be learned continuously. Therefore, we consider using an RL-based method to derive the optimal power allocation, which has been proved to be an effective method to solve the optimization problem [51]. Because the optimization parameter κ is continuous, we use proximal policy optimization (PPO) [52], which is a widely adopted method with the ability to handle the continuous action space.

6.3.1 Designed State Space, Action, and Reward function

To solve the problem (63), we define the state space, action, and reward function of the PPO as follows:

State: For each step t ($t = 1, 2, \dots, T$), the state s_t is defined as a union of $\{P_{max}, \Lambda, \xi_a^{*,t}, \bar{R}_1^t, \bar{R}_2^t\}$, where $\xi_a^{*,t}$, \bar{R}_1^t , and \bar{R}_2^t are the AMDEP, the ergodic public rate of B_1 , and the ergodic covert rate of B_2 , for this step, respectively.

Action: The action of the PPO policy at step t (a_t) is κ .

Reward: The reward observed at the end of each step is set as follows:

$$r_t = \begin{cases} 0, & \xi_a^{*,t} < 1 - \Lambda, \\ \bar{R}_1^t + \bar{R}_2^t, & \xi_a^{*,t} \geq 1 - \Lambda. \end{cases} \quad (64)$$

6.3.2 Basic Principles of PPO

Suppose that for any policy π , there exists a deterministic value function V_π corresponding to it [53]. The PPO algorithm can improve the strategy based on the feedback from the value function through strategy iteration without prior knowledge. The key idea behind strategy iteration is to

increase the probability of higher-rewarding actions through strategy evaluation and improvement while decreasing the likelihood of lower-rewarding action until the strategy maximizes the desired long-term reward is obtained. The policy and value function neural network parameters ϑ are used to parameterize the policy and value function. The strategy and value functions of the shared parameters are parameterized by the neural network ϑ . At each episode, a few mini-batches of experience in the replay buffer are randomly sampled to update the neural network parameters of the PPO. In PPO, $A(s, a)$ estimated with generalized advantage estimation [54] is used to train the state-value function $V(S)$. Then, the optimization objective, i.e., the long-term reward, is maximized by a stochastic gradient ascent method, and the policy and value function is updated accordingly, as follows:

$$\vartheta^{e+1} = \arg \max_{\vartheta} \frac{1}{D} \sum_D \mathbb{E}_k [L_k^A(\vartheta^e) - cL_k^{VF}(\vartheta^e)], \quad (65)$$

where the superscript of ϑ indicates the episode number, D is the number of iterations, c is the loss coefficient of the value function,

$$L_k^A(\vartheta^e) = \min[r_k^e(\vartheta^e)A(s^k, a^k), g(\epsilon, A(s^k, a^k))], \quad (66)$$

and

$$L_k^{VF}(\vartheta^e) = (V(s^k) - V_{target}^k)^2, \quad (67)$$

with

$$r_k^e(\vartheta^e) = \frac{\pi_{\vartheta^e}(a^k|o^k)}{\pi_{\vartheta^{e'}}(a^k|o^k)}, \quad (68)$$

$$A(s^k, a^k) = -V(s^k) + \sum_{l=k}^{K-1} \gamma^{l-k} R(s^l, a^l) + \gamma^{K-k} V(s^K), \quad (69)$$

and

$$g(\epsilon, A) = \begin{cases} (1 + \epsilon)A, & A \geq 0, \\ (1 - \epsilon)A, & A < 0. \end{cases} \quad (70)$$

Here, V_{target}^k is the total discount reward from step k to the end of episode, $\vartheta^{e'}$ represents the parameter of policy for sampling, r_k^e is the importance ratio.

6.3.3 The PPO-Based Algorithm for Power Allocation Optimization

Based on the principle of PPO and the optimization problem (63), we can design a PPO-based power allocation algorithm that maximizes the sum rate under the constraints.

Accordingly, the PPO-based power allocation algorithm is designed as shown in Algorithm 1. By using Algorithm 1, we can appropriately allocate power to Alice and Jammer so that the sum rate is maximized while the covertness performance is ensured. In particular, after the total reward converges, the action indicates the final power allocation coefficient, the state indicates the ergodic public rate and ergodic covert rate. Moreover, the computational complexity of the proposed algorithm is analyzed. In the proposed PPO-based power allocation algorithm, the input and output dimensions are determined, which are the dimensions of state space and action space, respectively, and can be ignored. Moreover, we use a multi-layer perceptron to parameterize the policy and value network. Therefore, the computational

Algorithm 1 PPO-based power allocation algorithm for covert RIS-NOMA networks

- 1: Initialize ϑ , P_{max} , Λ , $\xi_a^{*,t}$, \bar{R}_1^t , \bar{R}_2^t ;
- 2: **for** episode $e = 1, 2, \dots$, **do**
- 3: Reset replay buffer \mathcal{D} ;
- 4: **for** step $k = 1, 2, \dots$
- 5: Observe s_k ;
- 6: Input s_k into actor network ϑ^e and determine the current action a_k ;
- 7: Transit to a new state s_{k+1} and compute the reward r_k ;
- 8: Store transitions $\{s_k, a_k, s_{k+1}, r_k\}$ in \mathcal{D} ;
- 9: **end**;
- 10: Sample D transitions in \mathcal{D} ;
- 11: Update ϑ through (65);
- 12: **end**;
- 13: After the total reward converges, the corresponding action is the final power allocation coefficient κ .

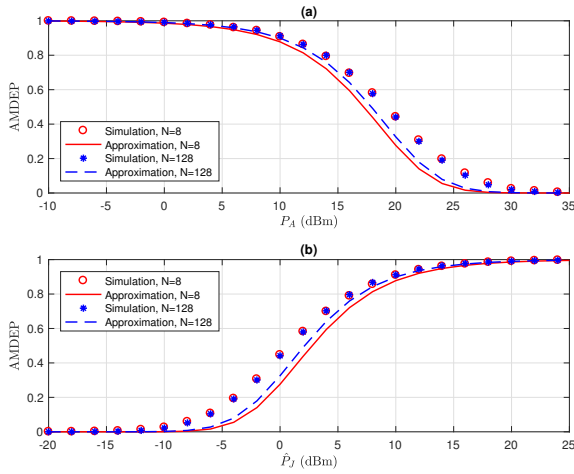


Fig. 2: AMDEP versus Alice's transmit power and Jammer's transmit power. (a) $\hat{P}_J = 10$ dBm. (b) $P_A = 10$ dBm.

complexity of the proposed algorithm is determined by the number of hidden layers L and the number of neurons H in each layer of the policy and value network, which can be expressed as $\mathcal{O}(HL)$.

6.4 Summary of Important Notations

Since there are many notations in this paper, we summarize them in Table 1 for ease of reading and understanding.

7 NUMERICAL RESULTS

In this section, the system performance is evaluated with numerical results. To verify the accuracy of analytical results, Monte Carlo simulation results are provided as well. The parameters setting is shown in Table 2 [9], [12].

7.1 Average Minimum Detection Error Probability

We plot the AMDEP curve of Willie versus the Alice's transmit power in Fig. 2(a), where the Jammer's transmit-power bound is fixed at 10 dBm, and the AMDEP curve

TABLE 1: Important notations

Variables	Definitions
\mathcal{L}_1	$L(d_{RB})L(d_{AR})$
\mathcal{L}_2	$L(d_{RB})L(d_{JR})$
\mathcal{L}_3	$L(d_{AB})$
\mathcal{L}_4	$L(d_{JB})$
\mathcal{L}_5	$L(d_{JW})$
\mathcal{L}_6	$L(d_{RW})L(d_{JR})$
\mathcal{L}_7	$L(d_{AW})$
\mathcal{L}_8	$L(d_{RW})L(d_{AR})$
ζ_1	$\mathcal{L}_5 h_{JW} ^2 + \mathcal{L}_6 \mathbf{h}_{RW}^T \mathbf{\Theta} \mathbf{h}_{JR} ^2$
ζ_2	$\mathcal{L}_7\alpha_1 P_A h_{AW} ^2 + \mathcal{L}_8\alpha_1 P_A \mathbf{h}_{RW}^T \mathbf{\Theta} \mathbf{h}_{AR} ^2 + \sigma_W^2$
ζ_3	$\mathcal{L}_7 P_A h_{AW} ^2 + \mathcal{L}_8 P_A \mathbf{h}_{RW}^T \mathbf{\Theta} \mathbf{h}_{AR} ^2 + \sigma_W^2$
τ_1	ζ_2
τ_2	$\zeta_1 \hat{P}_J + \zeta_2$
τ_3	ζ_3
τ_4	$\zeta_1 \hat{P}_J + \zeta_3$
η_1	$\frac{\mathcal{L}_6 \hat{P}_J}{\mathcal{L}_8 \alpha_2 P_A}$
η_2	$\frac{\mathcal{L}_5 \hat{P}_J}{\mathcal{L}_8 \alpha_2 P_A \beta^2}$
η_3	$\frac{\mathcal{L}_7}{\mathcal{L}_8 \beta^2}$
η_4	$\frac{\eta_1 m_{JW} m_{AW}}{(\eta_1 + 1) \Gamma(m_{JW}) \Gamma(m_{AW})} \left(m_{JW} - \frac{\eta_2}{N \eta_1} \right)^{-m_{JW}}$
η_5	$m_{AW} + \frac{\eta_3}{N \eta_1}$
η_6	$\frac{\eta_3 m_{JW}}{\eta_2} - \frac{\eta_3}{N \eta_1}$
η_7	$\frac{m_{AW}}{\Gamma(m_{AW})}$
η_8	$\frac{\eta_3}{\eta_2 N} + m_{AW}$
η_9	$\frac{m_{JW} m_{AW}}{(\eta_1 + 1) \Gamma(m_{JW}) \Gamma(m_{AW})} \left(\frac{\eta_2}{N} + m_{JW} \right)^{-m_{JW}}$
η_{10}	$m_{AW} - \frac{\eta_3}{N}$
η_{11}	$\frac{\eta_3}{N} + \frac{\eta_3 m_{JW}}{N}$
η_{12}	$\frac{m_{AW}^2}{\Gamma(m_{AW}) \Gamma(m_{JW})}$
η_{13}	$\frac{m_{JW} \eta_3}{m_{JW} \eta_3}$
ν_1	$\frac{\mathcal{L}_6 \hat{P}_J}{\mathcal{L}_8 \alpha_2 P_A} a$
ν_2	$\frac{\mathcal{L}_5 \hat{P}_J}{\mathcal{L}_8 \alpha_2 P_A \beta^2} a$
ν_3	$\frac{\mathcal{L}_7}{\mathcal{L}_8 \beta^2}$
ν_4	$\frac{\nu_1 m_{JW} m_{AW}}{(\nu_1 + 1) \Gamma(m_{JW}) \Gamma(m_{AW})} \left(m_{JW} - \frac{\nu_2}{N \nu_1} \right)^{-m_{JW}}$
ν_5	$m_{AW} + \frac{\nu_3}{N \nu_1}$
ν_6	$\frac{\nu_3 m_{JW}}{\nu_2} - \frac{\nu_3}{N \nu_1}$
ν_7	$\frac{m_{AW}}{\Gamma(m_{AW})}$
ν_8	$\frac{\nu_3}{\nu_2 N} + m_{AW}$
ν_9	$\frac{m_{JW} m_{AW}}{(\nu_1 + 1) \Gamma(m_{JW}) \Gamma(m_{AW})} \left(\frac{\nu_2}{N} + m_{JW} \right)^{-m_{JW}}$
ν_{10}	$m_{AW} - \frac{\nu_3}{N}$
ν_{11}	$\frac{\nu_3}{N} + \frac{\nu_3 m_{JW}}{N}$
ν_{12}	$\frac{m_{AW}^2}{\Gamma(m_{AW}) \Gamma(m_{JW})}$
ν_{13}	$\frac{m_{JW} \nu_3}{m_{JW} \nu_3}$

of Willie versus the Jammer's transmit power in Fig. 2(b), where the Alice's transmit power is fixed at 10 dBm. For both cases of $N = 8$ and $N = 128$, it is observed that the AMDEP decreases with P_A and converges to 0 for $P_A \rightarrow \infty$ as shown in Fig. 2(a), and increases with P_J and converges to 1 for $\hat{P}_J \rightarrow \infty$ as shown in Fig. 2(b). This phenomenon is reasonable since a larger ratio between the jamming power and the transmit power of B_1 's signal creates a larger uncertainty of Willie. We also observe that the number of RIS elements has little effect on AMDEP, since the jamming power and the nature of NOMA are the main factors affecting covertness performance. Additionally, in both subfigures, it is observed that the simulation results are well approximated by analytical results given by (51), especially for the range where the AMDEP is greater than

TABLE 2: Parameters setting

Bandwidth	$B = 1$ MHz
Number of RIS reflecting elements	$N = 8$ and 128
Amplitude-reflection coefficient of the RIS	$\beta = 0.9$
Distances	$d_{AB} = d_{JB} = 100$ m, $d_{AR} = d_{JR} = 110$ m, $d_{AW} = d_{JW} = 90$ m, and $d_{RB} = d_{RW} = 50$ m
Path-loss exponents	$\alpha_{AB} = \alpha_{JB} = 3$, $\alpha_{AR} = \alpha_{JR} = 2.5$, $\alpha_{AW} = \alpha_{JW} = 3$, and $\alpha_{RB} = \alpha_{RW} = 2.5$
Nakagami fading parameters	$m_{AB} = m_{JB} = 2$, $m_{AR} = m_{JR} = 3$, $m_{AW} = m_{JW} = 2$, and $m_{RB} = m_{RW} = 3$
NOMA power allocation coefficients	$\alpha_1 = 0.95$, $\alpha_2 = 0.05$
Noise power	$\sigma_1^2 = \sigma_2^2 = \sigma_W^2 = -80$ dBm
Number of points for Chebyshev-Gauss quadratures	$u_1 = u_2 = 100$
Number of points for Gauss-Laguerre quadrature	$u_3 = 100$

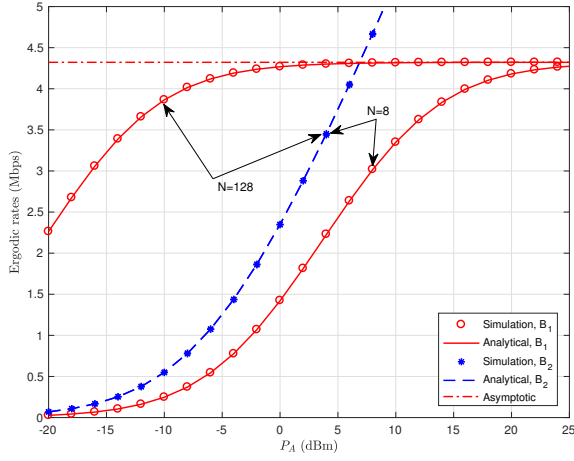


Fig. 3: The ergodic rates of B_1 and B_2 versus Alice's transmit power.

80%. This error is caused by the use of the central limit theorem (CLT)-based equivalent channel gains of RIS reflected links, and the similar phenomenon can be found in [12], [49]. Moreover, since the predefined DEP threshold is greater than 80%, the analytical results can be used in the optimization problem for power allocation.

7.2 Ergodic Public and Covert Rates

The transmissions of B_1 and B_2 are public and covert, respectively. Their ergodic public and covert rates versus the Alice's transmit power for $N = 8$ and $N = 128$ are depicted in Fig. 3. First, we observe that the simulation points for ergodic public and covert rates match well with the corresponding analytical results derived from (52) and (54), respectively. Then, we observe that the B_1 's ergodic public rate increases as P_A increases, and converges to (52). Meanwhile, the B_2 's ergodic covert rate always increases as P_A increases. Thus, the transmission of B_2 is more worthy of being covert. Furthermore, we observe that the increase in N leads to the increase in B_1 's ergodic rate before convergence, while it has no effect on B_2 's ergodic rate since B_2 is not assisted by the RIS. The correctness of analysis enables the analytical results to be used in the optimization problem for power allocation.

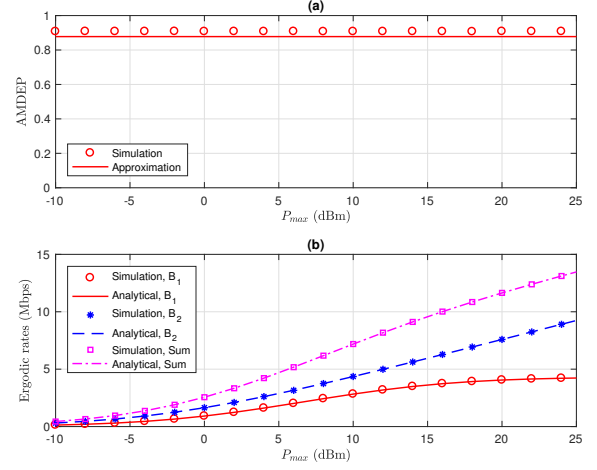


Fig. 4: AMDEP and ergodic rates versus P_{max} when $\kappa = 0.5$.

7.3 Fixed Power Allocation

For a fixed power allocation coefficient ($\kappa = 0.5$), we plot the AMDEP and the ergodic rates of two receivers versus P_{max} in Fig. 4. Since the number of N slightly affects the AMDEP and only affects B_1 's ergodic rate before convergence in the considered system, we evaluate performance for the case of $N = 8$ in the following. We observe that the AMDEP is not related to P_{max} , while both receivers' ergodic rates and the sum ergodic rate are affected by P_{max} . The former phenomenon is because the minimum DEP (29) is related to P_A/\hat{P}_J , and the AMDEP (its expectation) (51) is also related to it, not P_{max} . In particular, due to the principle of NOMA, the ergodic rate of B_1 converges to a value, while the ergodic rate of B_2 keeps increasing as the total power limit. Also, we observe that the AMDEP is 88% and the approximation error for the AMDEP is small for this case. Thus, when we optimize the power allocation in the following, the optimized κ for a P_{max} is applicable to other P_{max} .

Since we define the power allocation coefficient $\kappa = P_A/P_{max} = 1 - \hat{P}_J/P_{max}$ and aim to optimize it in (62), we first plot the AMDEP and ergodic rates of two receivers versus κ in Fig. 5. We first observe that the AMDEP decreases with κ . Specifically, although the approximation error for the AMDEP increases with κ , it is still acceptable. More importantly, it is well approximated for $\text{AMDEP} \geq 80\%$.

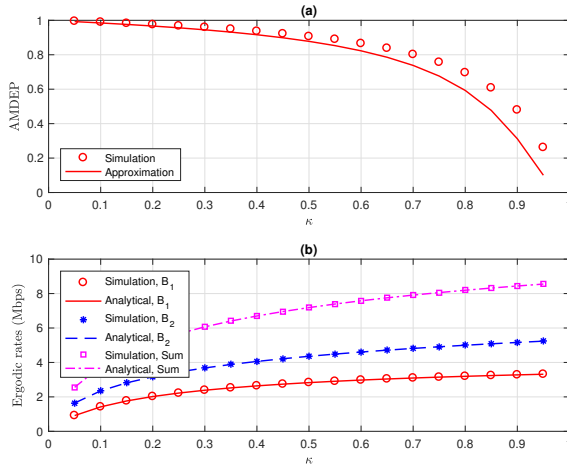


Fig. 5: AMDEP and ergodic rates versus κ when $P_{max} = 10$ dBm.

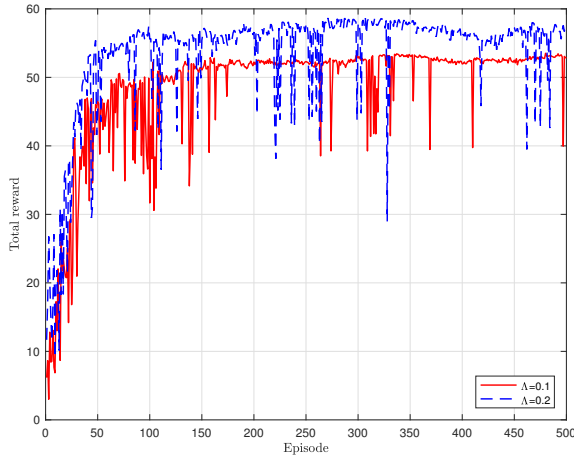


Fig. 6: Total reward versus episode in PPO when $P_{max} = 10$ dBm.

Since the threshold for AMDEP is usually set above 80%, the analytical result for the AMDEP can be used in the optimization problem. Then, we observe that both receivers' ergodic rates and the sum ergodic rate increases with κ , and our analytical results match well with the simulation results. Thus, the analytical results of ergodic rates can be used in the optimization problem as well.

7.4 Optimized Power Allocation

The training process of the PPO-based power allocation algorithm is plotted in Fig. 6. We observe that the total reward of PPO converges after 100 episodes. The convergence value for $\Lambda = 0.1$ is lower than that for $\Lambda = 0.2$, since lower Λ reveals the requirement of higher jamming power, which results in lower data rate. The converged action indicates the final power allocation coefficient, and the converged state implies the final achieved AMDEP and ergodic rates.

To show the effectiveness of the proposed PPO-based power allocation algorithm, we plot the sum rate versus

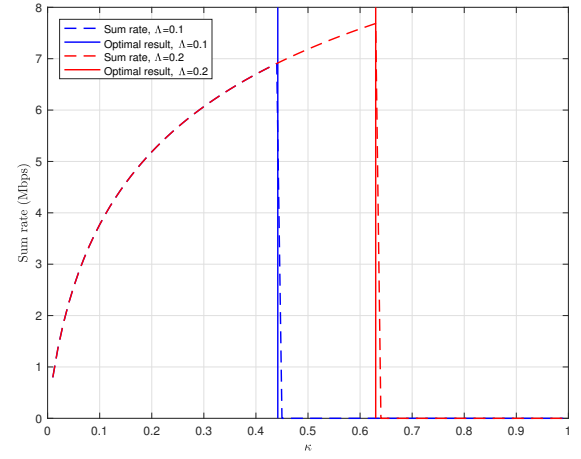


Fig. 7: Sum rate versus κ when $P_{max} = 10$ dBm.

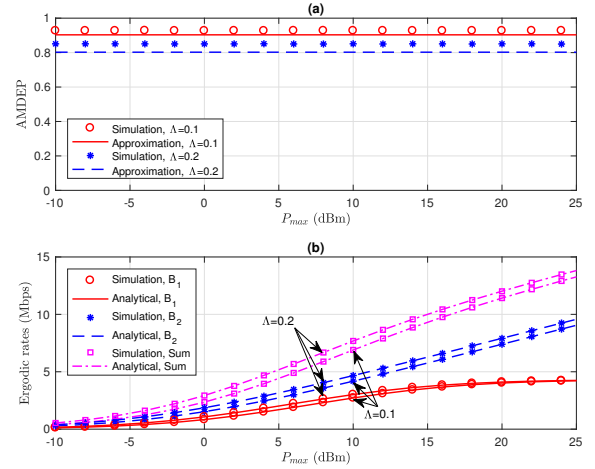


Fig. 8: AMDEP and ergodic rates versus P_{max} where κ is optimized.

the power allocation coefficient κ , and the final result of κ derived by the proposed algorithm in Fig. 7. Specifically, we define that the objective of the maximization problem (the sum rate) equals 0 when the constraint cannot be satisfied. We observe that the derived results for $\Lambda = 0.1$ and 0.2 are optimal, since both sum rates are maximized, which demonstrates the effectiveness the proposed PPO-based algorithm.

In Fig. 8, we plot the curves of AMDEP and ergodic rates after optimizing power allocation for Λ equals 0.1 and 0.2, respectively. It is first observed that the AMDEP is greater than 0.9 and 0.8 for Λ equals 0.1 and 0.2, respectively. It demonstrates that our proposed PPO-based power optimization algorithm is effective. Also, the maximized sum rates for these two cases are plotted. We observe that the sum rate for $\Lambda = 0.1$ is lower than that for $\Lambda = 0.2$. The reason is that a larger Λ indicates a lower AMDEP requirement, which results in a lower jamming power requirement, and thus, a higher sum rate is achieved. In a practical system, we can determine Λ based on the actual covertness demand

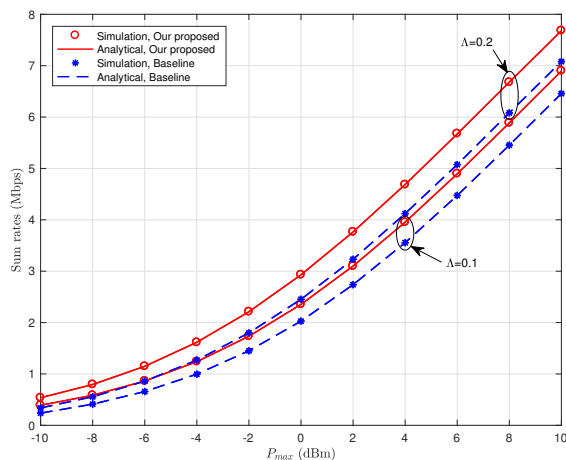


Fig. 9: Sum rate comparison under the proposed scheme and the baseline scheme.

of the system.

We can uniformly quantize the power allocation space to be discrete. As such, we can use traditional RL-based methods (e.g., Q-learning (QL) and deep Q-network (DQN)) for power allocation. Here, we use a QL-based power allocation method as the baseline [55], where the action space contains N_v uniform discrete values from 0 to 1. Then, we plot sum rates under our proposed PPO-based scheme and the baseline scheme ($N_v = 8$) in Fig. 9. We can observe that our proposed scheme can achieve higher sum rates than the baseline for $\Lambda = 0.1$ and $\Lambda = 0.2$. This phenomenon demonstrates the effectiveness of our proposed PPO-based power allocation scheme.

8 CONCLUSION

We have proposed jammer-aided covert RIS-NOMA communications and analyzed the corresponding performance. First, we have derived the closed-form expression for the AMDEP of Willie. Then, we have derived the closed-form expression for the ergodic rates of both NOMA receivers. Next, the power allocation is optimized by maximizing the sum rate while ensuring covertness performance. Simulations have demonstrated that the PPO-based power allocation scheme is effective. In this paper, the transmission of the stronger-signal receiver is protected, and it is worth investigating the realization of efficiently protecting both receivers' transmissions in a NOMA pair, which is an interesting future work.

REFERENCES

- [1] Y. Cheng, J. Lu, D. Niyato, B. Lyu, M. Xu, and S. Zhu, "Performance analysis of jammer-aided covert ris-noma systems," in *Proc. IEEE Global Commun. Conf. (GLOBECOM)*, Rio de Janeiro, Brazil, Dec. 2022, pp. 2716–2721.
- [2] Y. Ma, W. Liang, J. Li, X. Jia, and S. Guo, "Mobility-aware and delay-sensitive service provisioning in mobile edge-cloud networks," *IEEE Trans. Mobile Comput.*, vol. 21, no. 1, pp. 196–210, Jan. 2022.
- [3] Y. Liu, Y. Li, Y. Niu, and D. Jin, "Joint optimization of path planning and resource allocation in mobile edge computing," *IEEE Trans. Mobile Comput.*, vol. 19, no. 9, pp. 2129–2144, Sep. 2020.

- [4] L. Chen, C. Shen, P. Zhou, and J. Xu, "Collaborative service placement for edge computing in dense small cell networks," *IEEE Trans. Mobile Comput.*, vol. 20, no. 2, pp. 377–390, Feb. 2021.
- [5] Y. M. Saputra, D. T. Hoang, D. N. Nguyen, and E. Dutkiewicz, "A novel mobile edge network architecture with joint caching-delivering and horizontal cooperation," *IEEE Trans. Mobile Comput.*, vol. 20, no. 1, pp. 19–31, Jan. 2021.
- [6] N. Van Huynh, D. T. Hoang, D. N. Nguyen, and E. Dutkiewicz, "Joint coding and scheduling optimization for distributed learning over wireless edge networks," *IEEE J. Sel. Areas Commun.*, vol. 40, no. 2, pp. 484–498, Feb. 2022.
- [7] J. Liu, C. Zhang, K. Xue, and Y. Fang, "Privacy preservation in multi-cloud secure data fusion for infectious-disease analysis," *IEEE Trans. Mobile Comput.*, to be published.
- [8] B. A. Bash, D. Goeckel, D. Towsley, and S. Guha, "Hiding information in noise: Fundamental limits of covert wireless communication," *IEEE Commun. Mag.*, vol. 53, no. 12, pp. 26–31, Dec. 2015.
- [9] L. Lv, Q. Wu, Z. Li, Z. Ding, N. Al-Dhahir, and J. Chen, "Covert communication in intelligent reflecting surface-assisted NOMA systems: Design, analysis, and optimization," *IEEE Trans. Wireless Commun.*, vol. 21, no. 3, pp. 1735–1750, Mar. 2022.
- [10] Z. Ding, L. Lv, F. Fang, O. A. Dobre, G. K. Karagiannis, N. Al-Dhahir, R. Schober, and H. V. Poor, "A state-of-the-art survey on reconfigurable intelligent surface-assisted non-orthogonal multiple access networks," *Proc. IEEE*, vol. 110, no. 9, pp. 1358–1379, Sep. 2022.
- [11] M. Giordani, M. Polese, M. Mezzavilla, S. Rangan, and M. Zorzi, "Toward 6G networks: Use cases and technologies," *IEEE Commun. Mag.*, vol. 58, no. 3, pp. 55–61, Mar. 2020.
- [12] Y. Cheng, K. H. Li, Y. Liu, K. C. Teh, and H. V. Poor, "Downlink and uplink intelligent reflecting surface aided networks: NOMA and OMA," *IEEE Trans. Wireless Commun.*, vol. 20, no. 6, pp. 3988–4000, Jun. 2021.
- [13] H. Shen, W. Xu, S. Gong, Z. He, and C. Zhao, "Secrecy rate maximization for intelligent reflecting surface assisted multi-antenna communications," *IEEE Commun. Lett.*, vol. 23, no. 9, pp. 1488–1492, Sep. 2019.
- [14] Y. Cheng, K. H. Li, Y. Liu, K. C. Teh, and G. K. Karagiannis, "Non-orthogonal multiple access (NOMA) with multiple intelligent reflecting surfaces," *IEEE Trans. Wireless Commun.*, vol. 20, no. 11, pp. 7184–7195, Nov. 2021.
- [15] Q. Wu and R. Zhang, "Towards smart and reconfigurable environment: Intelligent reflecting surface aided wireless network," *IEEE Commun. Mag.*, vol. 58, no. 1, pp. 106–112, Jan. 2020.
- [16] Z. Ding, P. Fan, and H. V. Poor, "Impact of user pairing on 5G nonorthogonal multiple-access downlink transmissions," *IEEE Trans. Veh. Technol.*, vol. 65, no. 8, pp. 6010–6023, Aug. 2016.
- [17] X. Lu, E. Hossain, T. Shafique, S. Feng, H. Jiang, and D. Niyato, "Intelligent reflecting surface enabled covert communications in wireless networks," *IEEE Network*, vol. 34, no. 5, pp. 148–155, Sep./Oct. 2020.
- [18] Z. Li, M. Xu, J. Nie, J. Kang, W. Chen, and S. Xie, "NOMA-enabled cooperative computation offloading for blockchain-empowered Internet of things: A learning approach," *IEEE Internet Things J.*, vol. 8, no. 4, pp. 2364–2378, Aug. 2020.
- [19] Y. Mao, C. You, J. Zhang, K. Huang, and K. B. Letaief, "A survey on mobile edge computing: The communication perspective," *IEEE Commun. Surveys Tuts.*, vol. 19, no. 4, pp. 2322–2358, 4th Quarter 2017.
- [20] L. P. Qian, A. Feng, Y. Huang, Y. Wu, B. Ji, and Z. Shi, "Optimal SIC ordering and computation resource allocation in MEC-aware NOMA NB-IoT networks," *IEEE Internet Things J.*, vol. 6, no. 2, pp. 2806–2816, Apr. 2018.
- [21] Y. Wu, K. Ni, C. Zhang, L. P. Qian, and D. H. Tsang, "Noma-assisted multi-access mobile edge computing: A joint optimization of computation offloading and time allocation," *IEEE Trans. Veh. Technol.*, vol. 67, no. 12, pp. 12 244–12 258, Dec. 2018.
- [22] C. Huang, S. Hu, G. C. Alexandropoulos, A. Zappone, C. Yuen, R. Zhang, M. Di Renzo, and M. Debbah, "Holographic MIMO surfaces for 6G wireless networks: Opportunities, challenges, and trends," *IEEE Wireless Commun.*, vol. 27, no. 5, pp. 118–125, Oct. 2020.
- [23] L. Wei, C. Huang, G. C. Alexandropoulos, C. Yuen, Z. Zhang, and M. Debbah, "Channel estimation for RIS-empowered multi-user MISO wireless communications," *IEEE Trans. Commun.*, vol. 69, no. 6, pp. 4144–4157, Jun. 2021.

- [24] D. Mishra and H. Johansson, "Channel estimation and low-complexity beamforming design for passive intelligent surface assisted MISO wireless energy transfer," in *Proc. IEEE Int. Conf. Acoust., Speech and Signal Process. (ICASSP)*, Brighton, UK, May 2019, pp. 4659–4663.
- [25] Z.-Q. He and X. Yuan, "Cascaded channel estimation for large intelligent metasurface assisted massive MIMO," *IEEE Wireless Commun. Lett.*, vol. 9, no. 2, pp. 210–214, Feb. 2020.
- [26] Z. Wang, L. Liu, and S. Cui, "Channel estimation for intelligent reflecting surface assisted multiuser communications: Framework, algorithms, and analysis," *IEEE Trans. Wireless Commun.*, vol. 19, no. 10, pp. 6607–6620, Oct. 2020.
- [27] E. Björnson, Ö. Özdogan, and E. G. Larsson, "Intelligent reflecting surface versus decode-and-forward: How large surfaces are needed to beat relaying?" *IEEE Wireless Commun. Lett.*, vol. 9, no. 2, pp. 244–248, Feb. 2020.
- [28] J. Lyu and R. Zhang, "Spatial throughput characterization for intelligent reflecting surface aided multiuser system," *IEEE Wireless Commun. Lett.*, vol. 9, no. 6, pp. 834–838, Jun. 2020.
- [29] Z. Zhang, Y. Cui, F. Yang, and L. Ding, "Analysis and optimization of outage probability in multi-intelligent reflecting surface-assisted systems," 2019, *arXiv:1909.02193*. [Online]. Available: <https://arxiv.org/abs/1909.02193>
- [30] C. Huang, A. Zappone, G. C. Alexandropoulos, M. Debbah, and C. Yuen, "Reconfigurable intelligent surfaces for energy efficiency in wireless communication," *IEEE Trans. Wireless Commun.*, vol. 18, no. 8, pp. 4157–4170, Aug. 2019.
- [31] C. Huang, Z. Yang, G. C. Alexandropoulos, K. Xiong, L. Wei, C. Yuen, Z. Zhang, and M. Debbah, "Multi-hop RIS-empowered terahertz communications: A DRL-based hybrid beamforming design," *IEEE J. Sel. Areas Commun.*, vol. 39, no. 6, pp. 1663–1677, Jun. 2021.
- [32] A. Zappone, M. Di Renzo, F. Shams, X. Qian, and M. Debbah, "Overhead-aware design of reconfigurable intelligent surfaces in smart radio environments," *IEEE Trans. Wireless Commun.*, vol. 20, no. 1, pp. 126–141, Jan. 2021.
- [33] X. Yu, D. Xu, and R. Schober, "MISO wireless communication systems via intelligent reflecting surfaces," in *Proc. IEEE/CIC Int. Conf. Commun. China (ICCC)*, Changchun, China, Aug. 2019, pp. 735–740.
- [34] Q. Wu and R. Zhang, "Intelligent reflecting surface enhanced wireless network via joint active and passive beamforming," *IEEE Trans. Wireless Commun.*, vol. 18, no. 11, pp. 5394–5409, Nov. 2019.
- [35] T. Hou, Y. Liu, Z. Song, X. Sun, Y. Chen, and L. Hanzo, "Reconfigurable intelligent surface aided NOMA networks," *IEEE J. Sel. Areas Commun.*, vol. 38, no. 11, pp. 2575–2588, Nov. 2020.
- [36] J. Zhu, Y. Huang, J. Wang, K. Navaie, and Z. Ding, "Power efficient IRS-assisted NOMA," *IEEE Trans. Commun.*, vol. 69, no. 2, pp. 900–913, Feb. 2021.
- [37] M. Fu, Y. Zhou, and Y. Shi, "Intelligent reflecting surface for downlink non-orthogonal multiple access networks," in *Proc. IEEE Global Commun. Conf. (GLOBECOM)*, Waikoloa, HI, USA, Dec. 2019, pp. 1–6.
- [38] G. Yang, X. Xu, and Y.-C. Liang, "Intelligent reflecting surface assisted non-orthogonal multiple access," in *Proc. IEEE Wireless Commun. and Netw. Conf. (WCNC)*, Seoul, South Korea, May 2020, pp. 1–6.
- [39] Ö. Özdogan, E. Björnson, and E. G. Larsson, "Intelligent reflecting surfaces: Physics, propagation, and pathloss modeling," *IEEE Wireless Commun. Lett.*, vol. 9, no. 5, pp. 581–585, May 2020.
- [40] X. Zhou, S. Yan, Q. Wu, F. Shu, and D. W. K. Ng, "Intelligent reflecting surface (IRS)-aided covert wireless communications with delay constraint," *IEEE Trans. Wireless Commun.*, vol. 21, no. 1, Jan. 2022.
- [41] J. Kong, F. T. Dagefu, J. Choi, and P. Spasojevic, "Intelligent reflecting surface assisted covert communication with transmission probability optimization," *IEEE Wireless Commun. Lett.*, vol. 10, no. 8, pp. 1825–1829, Aug. 2021.
- [42] J. Si, Z. Li, Y. Zhao, J. Cheng, L. Guan, J. Shi, and N. Al-Dhahir, "Covert transmission assisted by intelligent reflecting surface," *IEEE Trans. Commun.*, vol. 69, no. 8, pp. 5394–5408, Aug. 2021.
- [43] C. Wang, Z. Li, J. Shi, and D. W. K. Ng, "Intelligent reflecting surface-assisted multi-antenna covert communications: Joint active and passive beamforming optimization," *IEEE Trans. Commun.*, vol. 69, no. 6, pp. 3984–4000, Jun. 2021.
- [44] H. Liu, X. Yuan, and Y.-J. A. Zhang, "Matrix-calibration-based cascaded channel estimation for reconfigurable intelligent surface assisted multiuser MIMO," *IEEE J. Sel. Areas Commun.*, vol. 38, no. 11, pp. 2621–2636, Nov. 2020.
- [45] L. Tao, W. Yang, S. Yan, D. Wu, X. Guan, and D. Chen, "Covert communication in downlink NOMA systems with random transmit power," *IEEE Wireless Commun. Lett.*, vol. 9, no. 11, pp. 2000–2004, Nov. 2020.
- [46] L. Tao, W. Yang, X. Lu, M. Wang, and Y. Song, "Achieving covert communication in uplink NOMA systems via energy harvesting jammer," *IEEE Commun. Lett.*, vol. 25, no. 12, pp. 3785–3789, Dec. 2021.
- [47] Y. Jiang, L. Wang, H. Zhao, and H.-H. Chen, "Covert communications in D2D underlaying cellular networks with power domain NOMA," *IEEE Syst. J.*, vol. 14, no. 3, pp. 3717–3728.
- [48] Q. Li, P. Ren, D. Xu, and Y. Xie, "Covert non-orthogonal multiple access vehicular communications with friendly jamming," in *Proc. IEEE Global Commun. Conf. (GLOBECOM) Workshops*, Taipei, Taiwan, Dec. 2020, pp. 1–6.
- [49] Z. Ding, R. Schober, and H. V. Poor, "On the impact of phase shifting designs on IRS-NOMA," *IEEE Wireless Commun. Lett.*, vol. 9, no. 10, pp. 1596–1600, 2020.
- [50] I. S. Gradshteyn and I. M. Ryzhik, *Table of Integrals, Series, and Products*, 7th ed. Amsterdam, The Netherlands: Elsevier, 2007.
- [51] D. Nguyen, M. Ding, P. Pathirana, A. Seneviratne, J. Li, and V. Poor, "Cooperative task offloading and block mining in blockchain-based edge computing with multi-agent deep reinforcement learning," *IEEE Trans. Mobile Comput.*, to be published.
- [52] J. Schulman, F. Wolski, P. Dhariwal, A. Radford, and O. Klimov, "Proximal policy optimization algorithms," 2017, *arXiv:1707.06347*. [Online]. Available: <https://arxiv.org/abs/1707.06347>
- [53] M. Xu, J. Peng, B. Gupta, J. Kang, Z. Xiong, Z. Li, and A. A. Abd El-Latif, "Multi-agent federated reinforcement learning for secure incentive mechanism in intelligent cyber-physical systems," *IEEE Internet Things J.*, vol. 9, no. 22, pp. 22 095–22 108, Nov. 2022.
- [54] J. Schulman, P. Moritz, S. Levine, M. Jordan, and P. Abbeel, "High-dimensional continuous control using generalized advantage estimation," 2018, *arXiv:1506.02438*. [Online]. Available: <https://arxiv.org/abs/1506.02438>
- [55] R. Amiri, H. Mehrpouyan, L. Fridman, R. K. Mallik, A. Nallanathan, and D. Matolak, "A machine learning approach for power allocation in HetNets considering QoS," in *Proc. IEEE Int. Conf. Commun. (ICC)*, Kansas City, MO, USA, May 2018, pp. 1–7.

Yanyu Cheng received the B.S.Eng. degree in information engineering from Shanghai Jiao Tong University, Shanghai, China, in 2015, and the M.Sc. degree in signal processing and the Ph.D. degree in electrical engineering from Nanyang Technological University (NTU), Singapore, in 2016 and 2021, respectively. He is currently a Post-Doctoral Research Fellow with Alibaba-NTU Singapore Joint Research Institute, NTU. His research interests include 5G/6G networks, cybersecurity, cloud computing, and machine learning.

Jianyuan Lu received the Ph.D. degree from the Department of Computer Science and Technology, Tsinghua University, in 2017. He got the B.S. degree from Information and Computing Science, Beijing University of Posts and Telecommunications, in 2011. He is currently a researcher in Alibaba Cloud. His research interests include cloud network measurements, cloud network anomaly detection, high performance network algorithm, and high performance cloud network forwarding.

Dusit Niyato (Fellow, IEEE) is a professor in the School of Computer Science and Engineering, at Nanyang Technological University, Singapore. He received the B.Eng. degree from King Mongkut's Institute of Technology Ladkrabang (KMUTL), Thailand in 1999 and the Ph.D. degree in Electrical and Computer Engineering from the University of Manitoba, Canada in 2008. His research interests are in the areas of sustainability, edge intelligence, decentralized machine learning, and incentive mechanism design.

Biao Lyu is the director of Department of Cloud Network Intelligence Operation in Alibaba Cloud. He is currently working toward the Ph.D. degree in Polytechnic at Zhejiang University, Hangzhou, China and his advisor is Dr. Peng Cheng. His research interests include large-scale virtual network control, big data analysis and machine learning for network and AIOps for network. He developed the first SDN controller in Alibaba Cloud Network and initiated intelligence cloud network platform project which turned to be the first big-data and machine learning based network operation platform 'Qitian' in Alibaba Cloud. The SDN controller controls millions of network devices in Alibaba Cloud while Qitian provides a simplified and effective network operation experience and ensures the reliability and efficiency of Alibaba Cloud Network. Before he joined Alibaba Cloud, he worked in Microsoft Windows team and focused on dynamic data center and hyper-v networking development.

Minrui Xu received the B.S. degree from Sun Yat-Sen University, Guangzhou, China, in 2021. He is currently working toward the Ph.D. degree in the School of Computer Science and Engineering, Nanyang Technological University, Singapore. His research interests mainly focus on mobile edge computing, deep reinforcement learning, and mechanism design.

Shunmin Zhu is the general manager of Department of Cloud Network in Alibaba Cloud. He is currently working toward the Ph.D. degree in Computer Science at Tsinghua University, Beijing, China and his advisor is Dr. Jiahai Yang. His research interests include large-scale virtual network measurement, large-scale network anomaly detection, cloud network architecture design, and network hardware offloading. He developed the Alibaba Cloud virtual network system "LuoShen", a large-scale cloud network architecture that supports over 20 data centers across the world, and connects tens of millions of virtual machines and all other Alibaba Cloud products. In the early work of Alibaba, he led to build a high-performance user-space network platform NetFrame, which has a 50 times single-core performance improvement than kernel-based forwarding. He also led to develop the DDos protection system called AliGuard, which safeguarded Alibaba e-commerce business from DNS flood attacks and synflood attacks for many years.